LLNL-JRNL-2007162

Lawrence Livermore National Laboratory

Exposing and Reducing Biases of Simulating Mixed-Phase Clouds in the Convection-Permitting E3SM Atmosphere Model: Lessons From an

Y Zhang, P Caldwell, M Zhang, L Lin, X Zheng, H Beydoun, P Wu, P Bogenschutz

February 2026

Journal of Geophysical Research: Atmosphere

Disclaimer

This work performed under the auspices of the U.S. Department of Energy by Lawrence Livermore National Laboratory under Contract DE-AC52-07NA27344.

JGR Atmospheres

RESEARCH ARTICLE
10.1029/2025JD044660

Special Collection:
The Energy Exascale Earth System Model (E3SM): Advancements in a Decade of Earth System Modeling

Exposing and Reducing Biases of Simulating Mixed-Phase Clouds in the Convection-Permitting E3SM Atmosphere Model: Lessons From an Arctic Cold-Air Outbreak

Lin Lin[1], Yunyan Zhang[1], Hassan Beydoun[1], Xue Zheng[1], Meng Zhang[1,2], Peter Bogenschutz[1], Peng Wu[3], and Peter M. Caldwell[1]

[1]Lawrence Livermore National Laboratory, Livermore, CA, USA, [2]Now at Department of Earth and Atmospheric Sciences, University of Houston, Houston, TX, USA, [3]Pacific Northwest National Laboratory, Richland, WA, USA

Key Points:

- Convection-permitting E3SM atmosphere model substantially underestimates supercooled liquid in Arctic cold cloud-topped mixed-phase clouds
- Modifying the subgrid cloud overlap treatment addresses the deficiency of supercooled liquid and improves cloud-top phase partitioning
- Micro- and macro-physics, and radiative properties of mixed-phase clouds are highly sensitive to treatments of ice nucleation processes

Supporting Information:

Supporting Information may be found in the online version of this article.

Correspondence to:

L. Lin and Y. Zhang,
lin58@llnl.gov;
zhang25@llnl.gov

Citation:

Lin, L., Zhang, Y., Beydoun, H., Zheng, X., Zhang, M., Bogenschutz, P., et al. (2026). Exposing and reducing biases of simulating mixed-phase clouds in the convection-permitting E3SM atmosphere model: Lessons from an arctic cold-air outbreak. *Journal of Geophysical Research: Atmospheres*, *131*, e2025JD044660. https://doi.org/10.1029/2025JD044660

Received 26 JUN 2025
Accepted 24 DEC 2025

Abstract Mixed-phase clouds modulate the water and energy cycles of high-latitude regions, yet their liquid-ice phase partitioning has long been poorly simulated in climate models. Here, simulations of Arctic mixed-phase clouds by the Simple Cloud-Resolving E3SM Atmosphere Model (SCREAM) are assessed against large-eddy simulations, satellite data, and ground-based observations during the Cold-Air Outbreaks in the Marine Boundary Layer Experiment field campaign. SCREAM simulates nearly completely frozen clouds, which is attributed largely to the unreasonably strong Wegener–Bergeron–Findeisen (WBF) process that converts liquid to ice excessively and partly to the early over-abundant ice production at cold temperatures from a temperature-deterministic deposition ice nucleation scheme. Assuming no subgrid variation for the WBF process in the original formulation particularly conflicts with the instantaneous saturation adjustment assumption in the condensation scheme that assumes subgrid variability, leading to exaggerated WBF process rates. A proposed simple physically-based improvement on the treatment of subgrid cloud overlap substantially increases supercooled liquid water content and notably improves cloud-top phase partitioning, aligning better with observations. Improvement of supercooled liquid water content also converges with increasing horizontal resolution. The deposition ice nucleation scheme is found responsible for a falsely-produced ice cloud aloft that is not observed, biasing the simulated cloud radiative effects and top-of-atmosphere radiative fluxes. This study identifies key deficiencies in cloud parameterizations that continue to challenge convection-permitting models.

Plain Language Summary Mixed-phase clouds that contain both supercooled liquid droplets and ice particles affect Arctic energy and water cycles and are essential for understanding current and future Arctic environment. However, the complex physical processes involving the interplay between liquid droplets and ice particles remain poorly understood and inadequately represented in computer models. In this study, the Department of Energy Simple Cloud-Resolving E3SM Atmosphere Model (SCREAM) is thoroughly evaluated in its ability to produce these so-called mixed-phase clouds by simulating a real marine cold-air outbreak case over the Norwegian Sea. SCREAM simulations are compared with a modeling benchmark, satellite measurements, and ground-based observations. Results show that SCREAM simulates predominantly frozen clouds, in contrast to observations that show a mix of liquid and frozen phases, with cloud microphysics parameterizations being a source of model errors. We propose potential avenues for model improvement. This work pinpoints the key physical processes driving modeling biases, informing improvements for next-generation km-scale models.

1. Introduction

Marine cold-air outbreaks (MCAOs) are common at high latitudes (Fletcher et al., 2016a), occurring when cold, dry polar air masses sweep off the sea ice edge over warm, moist open ocean (Pithan et al., 2018). Strong air-sea temperature contrast spurs intense surface heat and moisture fluxes, fueling cloud formation within the convective boundary layer. In particular, mixed-phase clouds are usually accompanying MCAOs (Fletcher et al., 2016b; Geerts et al., 2022). Thus, MCAOs serve as a natural laboratory for studying evolutionary mixed-phase clouds from a Lagrangian perspective (e.g., Zheng et al., 2024).

The Arctic cloud feedback and energy budget are found to closely link to mixed-phase cloud microphysical processes (e.g., Pithan et al., 2014; Tan & Storelvmo, 2019). For a global kilometer-scale convection-permitting model, SCREAM, to better inform Arctic climate change studies, it is necessary to evaluate the model's

performance and ability in simulating mixed-phase clouds. To achieve this goal, we investigate the representations of mixed-phase cloud microphysics in SCREAM from a cold-air outbreak during the Cold-Air Outbreaks in the Marine Boundary Layer Experiment (COMBLE) field campaign over the Norwegian Sea.

Despite their ubiquity and importance, accurately simulating mixed-phase clouds remains challenging for regional and global climate models, with a persistent bias of supercooled liquid water underestimation to a varying degree (Barrett et al., 2017; Klein et al., 2009; Komurcu et al., 2014). The modeling biases of the relative amount of liquid and ice phase have important implications, e.g., Tan et al. (2016) showed that underestimated supercooled liquid in mixed-phase clouds in the present days translates into an underpredicted warming in the future (i.e., too negative cloud phase feedback). Correcting for the low bias of supercooled liquid in better agreement with observations gives rise to a more sensitive earth system (Zelinka et al., 2020) with an alarming Arctic warming (Tan & Storelvmo, 2019). Accurately simulating liquid-ice phase partitioning in mixed-phase clouds is critical to enhance the credibility of a model.

The sources of uncertainties in simulating liquid-ice phase partitioning can be traced to the representations of two groups of processes: ice initiation and phase transition. Ice formation via heterogeneous ice nucleation triggered by ice nucleating particles (INPs) introduces the initial ice into the supercooled liquid clouds, a first step in the spontaneous formation of mixed-phase clouds. Therefore, liquid-ice phase partitioning exhibits high sensitivity to INP abundance, ice nucleation processes, and their parameterizations (Komurcu et al., 2014; Morrison, Shupe, et al., 2005). Tan and Barahona (2022) showed immersion freezing parameterizations that predict reasonably low INP concentrations produce a more realistic representation of liquid-ice phase in Arctic mixed-phase clouds. In other words, models with the widely used aerosol-unaware temperature-deterministic INP parameterizations (e.g., Bigg, 1953; Cooper, 1986; Meyers et al., 1992) that are found to overestimate INP concentrations by 1-2 orders of magnitude relative to measurements during CAOs (Irish et al., 2019; Welti et al., 2020) likely result in deficient supercooled liquid. The sources, concentrations, and life cycle of INPs within the Arctic marine boundary layer are highly uncertain (Geerts et al., 2022; Raatikainen et al., 2022; Raif et al., 2024). The adoption of the Arctic region-specific INP parameterization improves simulations of Arctic mixed-phase clouds and energy balance (Gjelsvik et al., 2024).

Accurate representations of phase transitioning processes following ice initiation are also critical for maintaining supercooled liquid water. Ice crystals once present have the propensity to grow at the expense of nearby evaporating liquid droplets, a process called the Wegener-Bergeron-Findeisen (WBF) process. Parameterizations of the WBF process conceptually involve a microphysics component that describes the process of vapor deposition onto ice, and a macrophysics component that describes the spatial mixing between liquid and ice. The latter is usually quantified as the mixed-phase cloud overlap/fraction. Uncertainties in both components affect WBF process rates. On the one hand, the WBF process is found to be overly efficient because subgrid liquid-ice spatial heterogeneity is inadequately represented. Airborne and space-borne measurements (Coopman & Tan, 2023; D'Alessandro et al., 2021; Evans et al., 2025; Korolev & Milbrandt, 2022; Sokol & Storelvmo, 2024) have shown inhomogeneous liquid and ice distributions, while many models usually assume uniform mixing in a given model grid box, resulting in overestimated liquid-ice contact and thus accelerating supercooled liquid depletion through the WBF process. Scaling down the WBF process rates to mimic the effect of considering the liquid-ice spatial heterogeneity increases the amount of supercooled liquid water (Zhang et al., 2019). Reducing the degree of horizontal spatial overlap of liquid-ice leads to an increase in the liquid water path (LWP) (Abel et al., 2017). Implementing a parameterization that considers heterogeneous liquid-ice mixing into the Community Atmospheric Model improves the modeled phase partitioning and cloud radiative forcing (Yang et al., 2025). On the other hand, Van Weverberg et al. (2023) showed cloud microphysics, rather than macrophysics, primarily drive low liquid water biases, with overactive vapor deposition onto snow being a key issue. Additionally, the remaining supercooled liquid can be consumed through riming, a process involving the collection of supercooled liquid droplets onto the ice crystal surface to produce rimed ice particles. Van Weverberg et al. (2023) reported that riming does not account for the low liquid bias in CAO mixed-phase clouds.

The desire to improve our understanding and modeling of mixed-phase clouds has motivated an increasing number of targeted field campaigns (e.g., Sorooshian et al., 2019; Verlinde et al., 2007; Wendisch et al., 2024). One of such, the Cold-Air Outbreaks in the Marine Boundary Layer Experiment (COMBLE) (Geerts et al., 2022) was conducted by the US Department of Energy (DOE) Atmospheric Radiation Measurement (ARM) program with a goal to better understand the properties of CAO mixed-phase clouds, their role in energy and water cycles.

COMBLE deployed the ARM Mobile Facility (AMF) at a coastal site in northern Norway (69°N) from December 2019 to May 2020. Ground-based observations during COMBLE, along with pixel-level satellite retrievals, provided rich observations of cloud mesoscale variations (Wu & Ovchinnikov, 2022) and cloud-scale processes (Lackner et al., 2023; Mages et al., 2023) for assessing the model performance in simulating Arctic mixed-phase clouds.

Based on observations collected during COMBLE, Zheng et al. (2024) examined cloud regime transition and microphysical properties in a MCAO over the Norwegian Sea using a 40-day simulation from the DOE SCREAM, and found that the underestimation of supercooled liquid and liquid water fraction persists. Zheng et al. (2024) speculated a few physical processes that are potentially responsible for the low bias of supercooled liquid including the oversimplified temperature-dependent ice nucleation process and too efficient WBF process. Testing these hypotheses is a main focus of this work. The goals of this study are to (a) assess the capability of SCREAM in simulating Arctic mixed-phase clouds under a marine cold air outbreak regime, (b) identify and elucidate the driver processes responsible for model biases, and (c) improve the physical representations of these driver processes based on ARM ground-based and satellite observations. To achieve these goals, we simulate a real MCAO case captured during the COMBLE field campaign using SCREAM's Doubly Periodic (DP-SCREAM) configuration (Bogenschutz et al., 2023) for efficient testing at the process-level. Sensitivity analyses include: (a) inhibition of deposition ice nucleation, (b) a modified subgrid liquid and ice cloud overlap treatment to make the microphysics and macrophysics assumptions more consistent, and (c) increasing model horizontal resolution from 3 km to 250 m.

2. SCREAM Model Physics

The Simple Cloud-Resolving E3SM Atmosphere Model (SCREAM) (Caldwell et al., 2021), capable of using Graphics Processing Unit (GPU) architectures to run efficiently at a global resolution of 3 km, is a new global convection-permitting model (GCPM) which alleviates many long-standing biases common in conventional low-resolution models. SCREAM includes non-hydrostatic fluid dynamics, a subgrid scale turbulence and cloud macrophysics scheme, a cloud microphysics scheme, a radiation scheme, an energy fixer, and a prescribed aerosol property functionality. The deep convection scheme is no longer required, as deep convective processes are now resolved in SCREAM. The model version employed in this study closely resembles SCREAMv0, as detailed in Caldwell et al. (2021).

Specifically, interactions between turbulence and boundary layer clouds are handled efficiently by the Simplified Higher Order Closure (SHOC) scheme, which is a unified cloud macrophysics, turbulence, and shallow convection parameterization centered around a double-Gaussian probability density function (Bogenschutz & Krueger, 2013). Cloud microphysics is mostly represented by the WRF version of the Predicted Particle Properties (P3) scheme (Morrison & Milbrandt, 2015), with modifications on the processes of vapor deposition, sublimation, and the associated WBF process and the use of fractional cloudiness to ensure compatibility with the rest of SCREAM (see Section 2.5 in Caldwell et al. (2021)).

2.1. Description of Microphysics and Macrophysics Parameterizations for Mixed-Phase Clouds

This section serves as a review of the parameterizations of fractional cloudiness, ice initiation, WBF, as well as vapor deposition onto ice in SCREAM. Though vapor depositional growth of ice occurs in pure ice clouds, we still discuss its parameterization because it is directly impacted when we modify the parameterization of WBF in mixed-phase clouds (see Section 2.2).

2.1.1. Parameterization of Cloud Fraction

Both SHOC and P3 schemes adopt the concept of fractional cloudiness. Subgrid-scale cloud fractions for liquid and ice are calculated separately. The liquid cloud fraction (CF_l) is provided by SHOC. The SCREAM employed in this study has adopted a mass-based ice cloud fraction scheme to diagnose ice cloud fraction (CF_i):

$$CF_i = \begin{cases} 1 & \text{if } q_i > 10^{-12} \text{ kg kg}^{-1} \\ 0 & \text{otherwise} \end{cases} \quad (1)$$

The original relative humidity-based ice cloud fraction scheme in SCREAMv0 is abandoned to address an inconsistency between ice cloud fraction and ice condensate mass (Caldwell et al., 2021). This all-or-nothing ice cloud fraction approach is more consistent with the settings in the C++ version SCREAM: SCREAMv1 (Donahue et al., 2024). In Section 2.1 of Donahue et al. (2024), it is pointed out that assuming the whole cell is filled with cloud whenever there is even a small amount of ice present is needed in order for P3 ice processes to be active for falling snow.

2.1.2. Mixed-Phase Cloud Initiation

Mixed-phase clouds usually originate from supercooled liquid clouds, where cloud liquid is produced by vapor condensation in the part of each grid cell where the total water mixing ratio exceeds the liquid saturation value as parameterized in SHOC, based on the instantaneous saturation adjustment assumption.

In SCREAM, heterogeneous ice nucleation is represented following the standard P3 microphysics scheme, which currently includes two mechanisms: immersion freezing — a freezing process involving an INP that becomes immersed in a supercooled droplet — and deposition nucleation, in which ice forms directly from vapor deposition on a dry INP surface. Immersion freezing of cloud droplets and raindrops is parameterized based on Bigg (1953) as a function of the droplet volume and cooling rate. Deposition ice nucleation follows the empirical formulation of Cooper (1986), where the ice crystal number concentration N_{ice} (L^{-1}) is given by

$$N_{ice} = 0.005 \times \exp[0.304 \times (273.15 - T)] \tag{2}$$

Deposition ice nucleation is triggered under conditions where temperature $T \leq 258K$ and ice supersaturation $S_i \geq 5\%$, and is limited to produce the maximum nucleated ice number to 100 L^{-1} in order to prevent unrealistically large numbers of ice particles for $T \leq 241K$.

2.1.3. Parameterizations of WBF and Vapor Deposition on Ice

In mixed-phase grid cells, ice will grow through WBF and riming which compete to deplete supercooled liquid. Additionally, ice will grow via vapor deposition, by which ice particles grow at the expense of water vapor. Vapor depositional growth of ice will proceed only when there is no co-existing supercooled liquid within the same grid cell. Below we focus on the parameterizations of WBF and vapor depositional growth.

The grid-mean WBF tendency rate is computed as

$$WBF_{\text{grid}} = \frac{q_{v,l} - q_{v,i}}{\Gamma_p \tau} \times \text{CF}_{\text{mp}}, \text{ where } \text{CF}_{\text{mp}} = \max(\text{CF}_{\text{i}}, \text{C}_{\text{Fl}}) \tag{3}$$

where $q_{\text{v,l}}$ and $q_{\text{v,i}}$ are in-cloud water vapor mixing ratio at liquid and ice saturation, respectively. SHOC's saturation adjustment assumption on liquid water implies that air in regions containing liquid is saturated with respect to liquid water after condensation is complete, which explains the use of $q_{\text{v,l}}$ to represent in-cloud water vapor mixing ratio in Equation 3. $q_{\text{v,i}}$ is computed at grid-scale temperature. $\Gamma_p = 1 + \left(dq_{v,i}/dT\right)(L_s/c_p)$ is the psychrometric correction to deposition associated with latent heating, c_p is the specific heat of air at constant pressure and L_s is the latent heat of sublimation. $\left(dq_{v,i}/dT\right)$ is the change of ice saturation vapor pressure with temperature. $\tau = 2\pi N_{0,i}\rho_a D_v \lambda_i^{-2}$ is the supersaturation relaxation time scale associated with ice deposition. ρ_a is air density, D_v is the diffusivity of water vapor in air, $N_{0,i}$ and λ_i are the intercept and slope parameters in the ice size distribution represented by gamma functions. The in-cloud tendency rate is multiplied with the mixed-phase cloud fraction CF_{mp} (see Section 2.1.4) to yield grid mean values.

The deposition of water vapor onto cloud ice proceeds with ice supersaturation and its rate is calculated similar to the WBF rate as

$$DEP_{\text{grid}} = \frac{q_v - q_{v,i}}{\Gamma_p \tau} \times \text{CF}_{\text{i}} \times (1 - ratio) \tag{4}$$

where q_v is the grid-mean water vapor mixing ratio. The in-cloud water vapor mixing ratio for vapor depositional growth of ice is assumed equal to the grid-mean value, following previous modeling practices (Gettelman et al., 2010; Morrison & Gettelman, 2008). While not capturing subgrid variability in water vapor, this simplification offers a straightforward and efficient approach. ratio $= min\left(\frac{q_l}{q_l \text{ sinks}}, 1\right)$ is the time adjustment factor representing the portion of a physics timestep during which supercooled liquid exists (q_l is the liquid water mass). For example, if supercooled liquid is not entirely depleted within a physics timestep (i.e., ql/ql sinks > 1), ratio is set to 1, and vapor depositional growth of ice does not occur. In some clouds that are originally mixed-phase, the liquid water is completely depleted (e.g., by WBF and/or riming) within a physics timestep (i.e., ql/ql sinks < 1). In such cases, vapor deposition onto ice proceeds for the remainder of that timestep when air is supersaturated with respect to ice (Equation 4). Sublimation occurs when the air becomes subsaturated with respect to ice. The in-cloud DEP tendency rate is multiplied with CF_i to yield grid mean values.

2.1.4. Treatment of Mixed-Phase Cloud Fraction

SCREAMv0 adopts the "maximum overlap" assumption of CF_{mp} being equal to the maximum between CF_i and CF_l (see Section 2.5 in Caldwell et al., 2021). For the remainder of the manuscript, we refer to this treatment as the subgrid cloud overlap. See Section 2.2 for details about the inconsistency between microphysics and macrophysics that arises from this subgrid cloud overlap assumption. No subgrid variability is assumed for liquid and ice when the two phases co-exist over CF_{mp}, similar to the "uniformly mixed" assumption discussed in Rotstayn et al. (2000, Figure 2). When liquid and ice are present in km-scale regions, they tend to be maximally overlapped (Evans et al., 2025). Such mixing assumption implies the largest possible depletion rate of liquid water via the WBF process that may deplete part or all of the liquid water in mixed-phase clouds.

2.2. Modifications on Mixed-Phase Cloud Fraction and Vapor Deposition on Ice

In cases with CF_i being larger than CF_l, inconsistency arises between macrophysics and microphysics when the aforementioned saturation adjustment assumption and CF_{mp} treatment are applied simultaneously. On the one hand, in-cloud WBF process rate is calculated assuming that the in-cloud water vapor mixing ratio is saturated with respect to liquid water. Importantly, this assumption is only valid within the areal extent of CF_l. On the other hand, the CF_{mp} treatment effectively adopts the assumption of liquid-ice uniformly mixed to the areal extent of a larger fraction. Note that the current SCREAM uses the all-or-nothing CF_i parameterization (see Section 2.1.1). Most of the time, CF_i will be 1 given the small ice mass threshold, indicating that nearly all CF_{mp} is set to 1. Consequently, the subgrid cloud overlap treatment systematically exaggerates the WBF process rate by applying the assumption of saturation with respect to liquid water over a broader area than actually diagnosed by SHOC. This overestimation is particularly pronounced when CF_i greatly exceeds CF_l. Because such assumptions may also be applied—perhaps unwittingly—in other weather and climate models, and given the frequent association between excessive WBF activity and the common low bias in supercooled liquid water, it is strongly recommended that model developers carefully inspect the coupling between macrophysics and microphysics in their own models. Ensuring consistency in the treatment of subgrid cloud overlap is critical for realistic simulation of mixed-phase cloud processes.

To address the gap, we propose a simple, computationally inexpensive remedy for the subgrid cloud overlap treatment. To maintain the validity of the assumption of in-cloud water vapor mixing ratio being saturated with respect to liquid and to ensure that the WBF process occurs over the actual liquid and ice overlap, we instead redefine CF_{mp} as the maximum overlap between liquid and ice. The grid-mean WBF tendency rate is revised as

$$WBF_{\text{grid}} = \frac{q_{v,l} - q_{v,i}}{\Gamma_p \tau} \times \text{CF}_{\text{mp}}, \text{where } \text{CF}_{\text{mp}} = \min(\text{CF}_i, \text{CF}_l) \tag{5}$$

Furthermore, we revise the treatment of vapor deposition onto ice accordingly as

$$DEP_{\text{grid}} = \frac{q_v - q_{vi}}{\Gamma_p \tau} \times \max(\text{CF}_i - \text{CF}_l, 0) + \frac{q_v - q_{vi}}{\Gamma_p \tau} \times \text{CF}_{\text{mp}} \times (1 - ratio) \tag{6}$$

In the case of a grid cell where CF_i is larger than CF_l, the grid cell contains (a) pure ice clouds occupying a fraction of CF_i-CF_l, and (b) mixed-phase clouds with a fraction of $CF_{mp} = \min(CF_l, CF_i)$. The process of vapor deposition onto ice thus consists of two parts: vapor deposition in pure ice clouds (first term) and in mixed-phase clouds (second term). Note that vapor deposition onto ice is now enabled before the entire depletion of liquid in a grid cell, which was not allowed previously. These modifications are physically sound and maintain generality for application to other cloud regimes (see Section 6.1). We therefore believe that model improvements extend beyond case-specific findings.

3. Numerical Experiment Details

3.1. Case Description

A prominent cold-air outbreak occurring on 13 March 2020 over the Norwegian Sea is the target case of the ongoing COMBLE Model-Observation Intercomparison Project (COMBLE-MIP, https://arm-development.github.io/comble-mip/README.html). This study simulates Arctic mixed-phase clouds embedded in this event and the findings of this work add to the COMBLE-MIP effort.

In Figure 1a, the satellite imagery vividly depicted the broad spectrum of cloud fields stretching more than 1,000 km from the ice edge north of Svalbard to the COMBLE ARM Mobile Facility (AMF) site in Andenes, Norway in about 18 hr: overcast boundary layer clouds (termed as overcast regime, denoted by a red box in Figure 1a), and subsequent cloud streets along the prevailing northerly wind (termed as roll regime, blue box) and a gradual transition into cellular convective clouds farther downstream (termed as cell regime, green box), exhibiting classical MCAO evolution patterns (Brümmer, 1999; Fletcher et al., 2016b; Pithan et al., 2018). In the vertical, clouds gradually deepen from near the surface off the sea-ice edge to about 4 km deep downstream (Figure 1b) over progressively warmer ocean surface (Figure 2a), as shown in the CALIPSO 532 nm attenuated backscatter signal along a transect that aligns with the MCAO trajectory (Figure 1b, read from right to left). These deepening clouds contain both liquid and ice, forming typical mixed-phase structures (Figure 1c).

Figure 2a shows the time-varying sea surface temperature (SST) along the air mass trajectory from the fifth generation European Center for Medium-Range Weather Forecasting atmospheric reanalysis (ERA5) (Hersbach et al., 2020). For the first 2 hr over Arctic sea ice, the surface remains at 247 K. From 2 to 4 hr immediately off the ice edge, SST abruptly rises by 25 K, then steadily increases from 275 to 280 K over 4–20 hr as air masses move toward the coast of Norway. The strong temperature contrast between cold air and warm ocean has made the 13 March 2020 case being characterized by large surface sensible and latent heat fluxes (Figures 2b and 2c), peaking at 770 W m^{-2} and 350 W m^{-2}, respectively, before decreasing to 110 W m^{-2} and 120 W m^{-2}. The intensity of a cold-air outbreak is quantified by the cold-air outbreak index $M \equiv \theta_{SST} - \theta_{800hPa}$, following Fletcher et al. (2016a), where θ_{SST} and θ_{800hPa} are the potential temperature at skin surface and 800 hPa, respectively. M is a measure of the thermal instability of the boundary layer driven by surface heat fluxes (positive values define an absolutely unstable lower troposphere). The 13 March case witnessed the highest M during COMBLE (Figure 2d).

3.2. DP-SCREAM Configuration

We simulate the 13 March case using the doubly-periodic configuration of SCREAM—referred to as DP-SCREAM (Bogenschutz et al., 2023) which enables model debugging, evaluation, tuning, and parameterization implementation in an efficient fashion. Functionally similar to a single-column model often used in global climate modeling, DP-SCREAM offers significantly low computational cost while maintaining the full suite of SCREAM's physics and dynamics. Importantly, DP-SCREAM has been shown to reproduce many of the same biases observed in SCREAM's global simulations, making it a reliable tool for isolating and diagnosing model behavior. Although SCREAM has since been ported to C++/Kokkos to support GPU acceleration (SCREAMv1; Donahue et al., 2024), the recently released DP-SCREAMv1 (Bogenschutz, Clevenger, et al., 2025) was not ready for scientific application at the time this study was conducted. In this study, we still use DP-SCREAMv0 (Fortran version) to investigate the key microphysical and macrophysical processes governing mixed-phase clouds (see Section 2.1), and to evaluate the effects of model code adjustments aimed at improving consistency of subgrid-variability assumptions (see Section 2.2). Bogenschutz, Clevenger, et al. (2025) demonstrate that the results from DP-SCREAMv0 and DP-SCREAMv1 are characteristically similar and scientifically indistinguishable. Throughout this manuscript, we refer to DP-SCREAMv0 as DP-SCREAM for simplicity unless otherwise

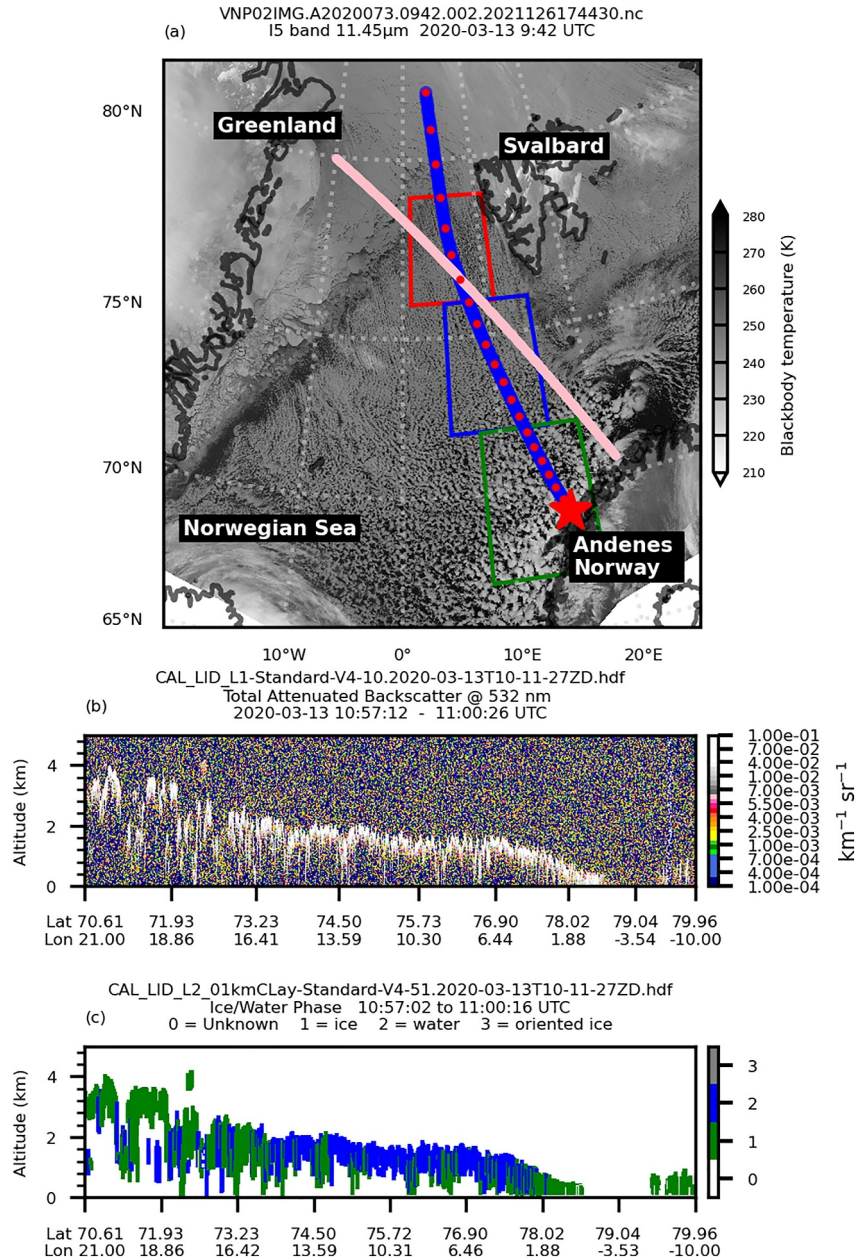

Figure 1. (a) A cold-air outbreak over the Norwegian Sea was captured by the Visible Infrared Imaging Radiometer Suite I5 band (11.45 μm) at 9:42 UTC on 13 March 2020. The Lagrangian trajectory of cold air mass is denoted by the blue line, extending from over the sea-ice at 81.69°N, 3.79°E to the ARM mobile facility site (69.14°N, 15.68°E, marked by a red star), with red dots for hourly intervals from 2020-03-12 22:00 UTC to 2020-03-13 18:00 UTC. The pink line shows the location of the satellite transect in (b) and (c) acquired by the cloud-aerosol LiDAR with orthogonal polarization. Red box denotes the overcast regime; blue box for the roll regime and green box for the cell regime. (b) shows the 532 nm total attenuated backscatter power while (c) for liquid and ice footprints with 1,308 pixels along the transect. The liquid-ice phase data are further used in the cloud top phase partitioning analysis shown in Figure 11.

specified. The 13 March 2020 COMBLE case has now been added to the DP-SCREAM case library and an initial assessment using DP-SCREAM was done by Bogenschutz, Zhang, et al. (2025).

Despite the high efficiency of DP-SCREAM, conducting a comprehensive set of simulations with fine grid spacing over a 1,000 km domain to cover the entire MCAO cloud fields is computationally impractical. To overcome this difficulty, the model is employed in a Lagrangian framework with manageable domain size. That is

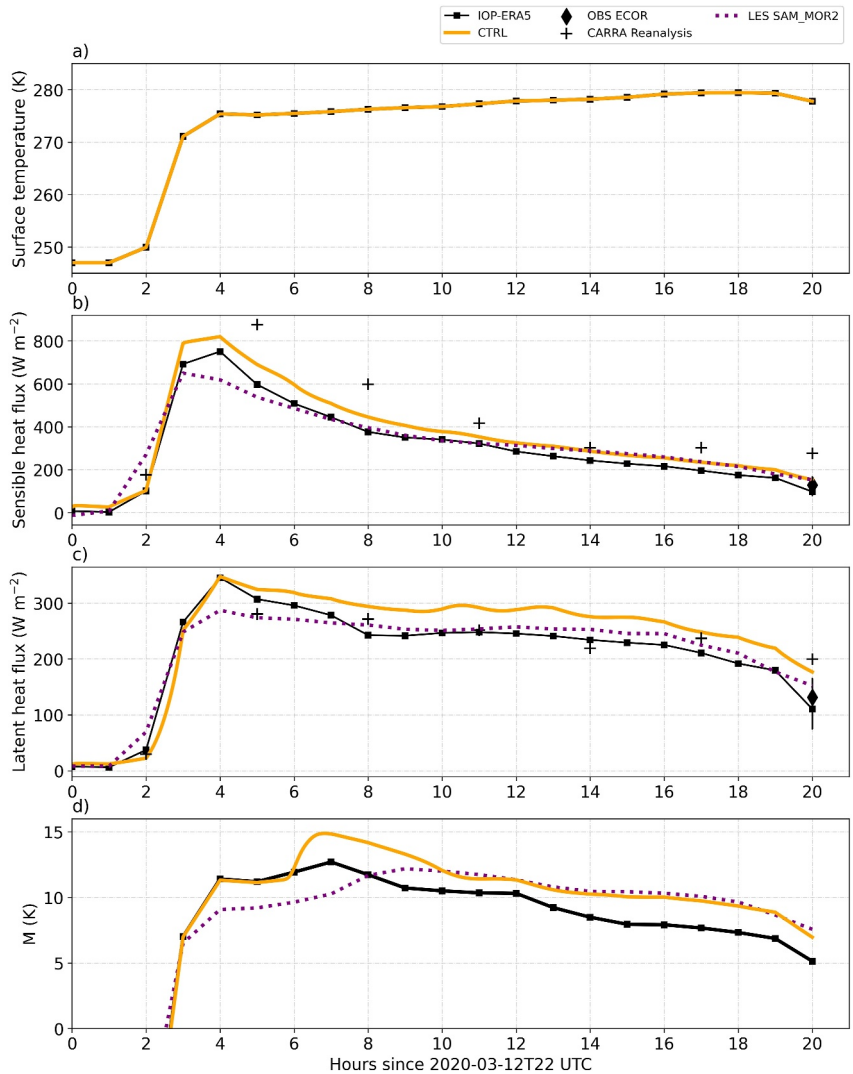

Figure 2. Time evolution of the domain mean (a) sea surface temperature, (b) sensible heat fluxes, (c) latent heat fluxes, and (d) cold-air outbreak index *M* along the Lagrangian trajectory of the 13 March 2020 cold-air outbreak from the default model simulations (yellow solid lines). Also shown are the surface forcings from ERA5 (black dotted lines) and Copernicus Arctic Regional Reanalysis (CARRA, denoted by crosses), observations at the ARM mobile facility site (denoted by diamonds), and results from large eddy simulations (purple dotted lines).

a stationary model domain forced with spatiotemporally varying boundary conditions translated along the cold air mass trajectory. We use a domain size of $(200\ \text{km})^2$ that is deemed large enough to capture the upscale growth of convective cells. A backward trajectory initiated at 1800 UTC, 13 March 2020 for air masses observed at the AMF site traces the origin of the cold air masses over the sea ice edge (blue line in Figure 1a). Hourly vertical profiles of meteorological variables (e.g., potential temperature, specific humidity, and wind) from ERA5 are extracted at the air mass origin to drive DP-SCREAM to run forward for 20 hr without nudging. Hourly SSTs from ERA5 along the trajectory (Figure 2a) are used to prescribe DP-SCREAM for interactive surface sensible and latent heat fluxes (Figures 2b and 2c). The setup of DP-SCREAM follows the protocol of COMBLE-MIP. Details about simulation specifics, initial condition soundings, and forcing information can be found in the COMBLE-MIP documentation at https://arm-development.github.io/comble-mip/README.html. For this case, SCREAM is configured to run with the default horizontal resolution of 3.25 km and 128 vertical layers that have a representative grid spacing of ~50 m in the boundary layer (Caldwell et al., 2021, Figure 1). The physics timestep is 75 s.

Table 1
Summary of Experiment

Experiment	Description
CTRL	Control simulation using the default DP-SCREAMv0 model
NOICE	As CTRL, but without all ice-relevant microphysical processes
NODEP	As CTRL, but without the deposition ice nucleation process
DEP130	As CTRL, but increase the ice supersaturation threshold triggering the deposition ice nucleation process from 105% to 130%
CLDFRAC	As CTRL, but modify the cloud overlap assumption used in the microphysics scheme (see Section 2.2)
ALLMOD	Combine all changes in NODEP and CLDFRAC
HR250 m	As CTRL, but increase model horizontal resolution to 250 m

3.3. Experiment Designs

A summary of model experiments is given in Table 1. Simulations with a range of sensitivity tests on key cloud microphysical processes are performed. Additionally, we conduct a sensitivity experiment using horizontal resolution of 250 m (with a physics timestep of 10 s) to test two hypotheses proposed for understanding the model behavior in the 3 km simulations. We speculate that supercooled liquid water underestimation associated with the subgrid cloud overlap treatment would vanish as model horizontal resolution becomes finer, and the erroneous ice cloud layer (Section 5.2) associated with the deposition ice nucleation scheme would persist regardless of model horizontal resolution. Apart from the horizontal resolution, the model setup is consistent across both the 250 m and 3 km simulations.

4. Data and Comparion With Model

It is noted that the range of suitable observational data sets is limited for comparison with a short-duration simulation of a specific MCAO event in the remote Arctic Ocean. Thus, we take advantage of a suite of satellite and ground-based observations. A large-eddy simulation is also set up, serving as a modeling benchmark for assessing simulations from SCREAM. We compare the simulated cloud properties with satellite observations over the open ocean and with the ground-based measurements acquired during the COMBLE field campaign on the Norwegian coast. A list of the reference data sets is summarized in Table A1.

4.1. Satellite Data Sets

- We visualize the cloud patterns for the 13 March MCAO event (Figure 1a) by converting the observed radiance data from visible infrared imaging radiometer Suite to blackbody temperature based on Planck's function.
- We use the hourly column-integrated total liquid (cloud and rain water combined) from MAC-LWP that is spatially and temporally collocated with the Lagrangian trajectory of cold air mass to produce domain-mean values for comparison with the simulated total LWPs. We average model LWPs including cloudy and clear regions to be consistent with the retrievals that are gridbox average estimates of all scenes (including clear sky conditions).
- The retrieved ice water path (IWP) from 2C-ICE in pixels spatially and temporally closest to the Lagrangian trajectory is used to assess the simulated ice condensate. We only include data within a up to three-hour window of the corresponding simulation time. As a result, only one data point (latitude: 78.75, longitude: 6.34 from 2020073031436_73914_CS_2C-ICE_GRANULE_P1_R05_E09_F00.hdf) is included for around 01:30 UTC on 13 March 2020. Note that model domain-mean IWP is qualitatively compared to a data point with horizontal resolution of approximately 1 km along the satellite's track. The modeled IWP includes precipitating ice (snow and graupel) to be consistent with satellite retrievals.
- IWP estimates from the chalmers cloud ice climatology (CCIC) ice cloud data set that ideally complements the sparse sampling of IWP from 2C-ICE are used for comparison with the simulated IWP near the Norwegian coast. CCIC data set with pixel resolution comparable to DP-SCREAM's horizontal resolution are still

averaged within an area comparable to the model domain size for comparison to model domain-mean values to obtain meaningful statistical significance.

- We derive the cloud-top supercooled liquid fraction (SLF) using the CAL_LID_L2_01kmCLay-Standard-V4-51 product that reports cloud layers of liquid and ice phase footprints for comparison with model counterparts. Observed SLFs are calculated as the ratio of the number of liquid pixels to the total number of liquid and ice pixels from the highest layer of the identified cloud tops. Simulated SLFs are calculated using the ratio of liquid to total (liquid + ice) mass mixing ratios, as the model lacks a direct analog to LiDAR backscatter footprint counts. Modeled cloud top is determined specifically at the highest level where total cloud mixing ratio ($qc + qi$) > 10^{-4} g kg^{-1} in the mixed-phase temperature ranges. Results from a model layer are used, despite that the model vertical resolution varies from about 50 m within the boundary layer to about 300 m at 500 hPa. We focus our comparison particularly on the low cloud tops (model vertical resolution comparable to that of Cloud-Aerosol LiDAR with Orthogonal Polarization (CALIOP) LiDAR) and make a qualitative comparison for high cloud tops (model vertical resolution much coarser than that of CALIOP LiDAR). The CAL_LID_L2_01kmCLay-Standard-V4-51 data set having pixel-level resolution similar to DP-SCREAM's horizontal resolution is compared directly to model column values.
- CERES_SYN1deg-1Hour_Ed4A data set spatially and temporally collocated with the Lagrangian trajectory produces domain-mean top of the atmosphere (TOA) longwave outgoing radiative fluxes, cloud radiative effects and IWP for model evaluation.

4.2. COMBLE Field Campaign Data Sets

A suite of ground-based observations collected at 18 UTC 13 March 2020 from the AMF site during the COMBLE field campaign (https://armgov.svcs.arm.gov/research/campaigns/amf2019comble) is integrated to evaluate the simulated surface heat fluxes and cloud properties when the cold air mass arrives the site. Hourly average data from both observations and simulations are compared. Specific data information is as follows:

- Surface sensible and latent heat fluxes are from the hourly averaged quality controlled eddy correlation Flux Measurement.
- The retrieved column-integrated total liquid by a microwave radiometer from the "anxmwrret1liljclouM1" data stream is used for comparing with the simulated total LWP.
- Estimates of cloud boundaries (i.e., cloud top height) are from the ARSCLKAZRBND1KOLLIAS data stream based on 35 GHz Ka-band ARM Zenith-pointing Radar, micropulse LiDAR, and ceilometer data.

4.3. Data From SAM LES

The large eddy simulation (LES) model used in this study is the System for Atmospheric Modeling (SAM) (Khairoutdinov & Randall, 2003) version 6.10.11. The simulation is run in the same quasi-Lagrangian framework as described for the DP-SCREAM. The hourly vertical profiles of meteorological variables from ERA5 are used to drive the LES model without nudging. Time- and height-varying pressure gradient forcing via geostrophic wind is used as large-scale forcing, with subsidence from the vertical velocity of ERA5. The model uses a two-moment microphysics scheme (Morrison, Curry, & Khvorostyanov, 2005) with prescribed cloud condensation nuclei number concentration of 20 cm^{-3} (Wu et al., 2025). N_{ice} is maintained near a prescribed value of 25 L^{-1} within the mixed-phase cloud (Ovchinnikov et al., 2014). Specifically, when the temperature is below 0 °C, the liquid water mixing ratio $q_l \geq 0.001$ g kg^{-1} and the fractional supersaturation over ice $S_i \geq 5\%$, if N_{ice} is below 25 L^{-1}, then new ice crystals are produced at a rate $\frac{\partial N_{ice}}{\partial t} = \frac{25\ \mathrm{L}^{-1} - N_{ice}}{\Delta t}$, where Δt is the model time step that is set to 1 s. Primary ice nucleation or secondary ice production mechanisms leading to ice particle formation are not specified. Once formed, ice particles grow only through the deposition of water vapor that is directly related to supersaturation. The WBF process is not explicitly represented through ice mass growth, but included in the calculation of the differential supersaturation ($\delta = q_v - q_{vl}$) with time as $\left(\frac{\partial \delta}{\partial t}\right)_{WBF} = -\frac{Q_1}{\Gamma_p}\frac{q_{v,l} - q_{v,i}}{\tau}$, where $Q_1 = 1 + \left(dq_{v,l}/dT\right)(L_s/c_p)$. The longwave radiative cooling rate is parameterized as a function of q_l profile as detailed in Ovchinnikov et al. (2014). The domain size for the LES simulation is (25.6 km)^2 with horizontal grid spacings of $\Delta x = \Delta y = 100$ m. The vertical grid spacing varies from $\Delta z = 20$ m near the surface to $\Delta z = 40$ m up to 5.5 km and $\Delta z = 80$ m upward, with the model top at 7 km.

5. Causes of Supercooled Liquid Water Underestimation

In the following subsections, we document the behavior of SCREAM in simulating Arctic mixed-phase clouds in comparison with LES and observations, and discuss model sensitivities to modified physics including treatments of subgrid cloud overlap and ice nucleation processes, as well as the sensitivity to model horizontal resolution.

5.1. Supercooled Liquid Water Underestimation

DP-SCREAM reproduces the gradual deepening of marine boundary layer cloud as air masses move away from the sea-ice edge (Figure 3), consistent with satellite observations (Figure 1b). Within these boundary layer clouds, DP-SCREAM also simulates liquid-ice mixed-phase features, in a qualitative agreement with the CALIOP pixel-level liquid-ice phase footprints that show liquid and ice mixtures along the 2D curtain across the MCAO cloud transitions (Figure 1c). However, the simulated mixed-phase clouds are nearly completely frozen (Figure 3c). The additional ice cloud layer above the boundary layer cloud will be discussed in Section 5.2.

Figure 4 shows time series of the simulated domain-mean liquid and ice water paths vertically integrated within the mixed-phase temperature ranges, as compared to observations and results from LES. LES simulated liquid and ice water paths agree relatively well with observations. However, the simulated LWP from the default SCREAM (CTRL) is smaller than that of the observed and LES by nearly one to two orders of magnitude over the whole simulation period. Tomassini et al. (2017) showed that the systematic underestimation in total cloud condensate (liquid + ice) could be due in part to the underpredicted surface fluxes. However, Figure 2 shows that DP-SCREAM is well constrained to reproduce the surface heat fluxes reported by reanalyzes, observations, and LES. Moreover, the simulated IWP generally agrees with observations, despite large uncertainties among observations. Thus, the underestimation of LWP in CTRL is more likely caused by cloud parameterizations.

Combined results from CTRL and a sensitivity experiment in which the whole set of ice microphysics is deactivated (the NOICE experiment) suggest that the interaction between liquid- and ice-phase microphysics, rather than the warm rain processes, is mainly responsible for the substantial underestimate of LWP in CTRL (Figure 5), consistent with previous findings (Abel et al., 2017; Klein et al., 2009). When only warm rain processes are considered (NOICE), the simulated LWP that excludes rainwater is still higher than the observed value (Figure 5). This indicates that the underestimated LWP is unlikely due to insufficient liquid condensation or too efficient warm rain processes. However, when ice-phase microphysical processes are included (CTRL), the LWP becomes substantially underestimated. Including rainwater in the calculations of LWP as an upper bound in the CTRL experiment does not resolve the low bias in the simulated LWP.

5.1.1. Role of Wegener–Bergeron–Findeisen (WBF) Process

A budget analysis of liquid water sources and sinks from the perspective of microphysical processes reveals that Wegener–Bergeron–Findeisen (WBF) accounts for more than 95% of the supercooled liquid water loss, the dominant mechanism depleting supercooled liquid water produced by condensation in SHOC (Figure 6a). Riming plays a trivial role in depleting supercooled liquid while contributions from the other microphysical processes are negligible.

The unexpectedly large WBF process rate warrants further investigation. Examination of the model source code leads to the discovery of an inappropriate subgrid cloud overlap assumption (Section 2.2). This specific 13 March case is a typical "mode A" CAO (Geerts et al., 2022), characterized by high M values, high cloud tops, strong convective cells, low LWP on average, and especially broken cloud cover. CF_l remains around 10%–20% across all three cloud regimes, though CF_i is around 100% by design (see Figure 7). Given the current setting, the WBF process rate is over-predicted by a factor of approximately 10 on average. In the case of grid cells where CF_i is larger than CF_l, the treatment of subgrid cloud overlap between liquid and ice for microphysics would adopt the larger cloud fraction in the WBF process formulation (see Equation 3 and Section 2.1.4), resulting in excessively efficient WBF processes. The assumption of in-cloud water vapor mixing ratio equal to the liquid saturation mixing ratio breaks when applied beyond the limited area occupied by liquid clouds. This overestimation of liquid-to-ice conversion arises mainly because of the inconsistent microphysics and macrophysics.

Although the root cause of the overly active WBF process is subtle, the solution we propose is straightforward, as detailed in Section 2.2. The WBF process is revised to be strictly constrained within the liquid fractional cloudiness, ensuring consistency with the instantaneous saturation adjustment assumption for liquid water.

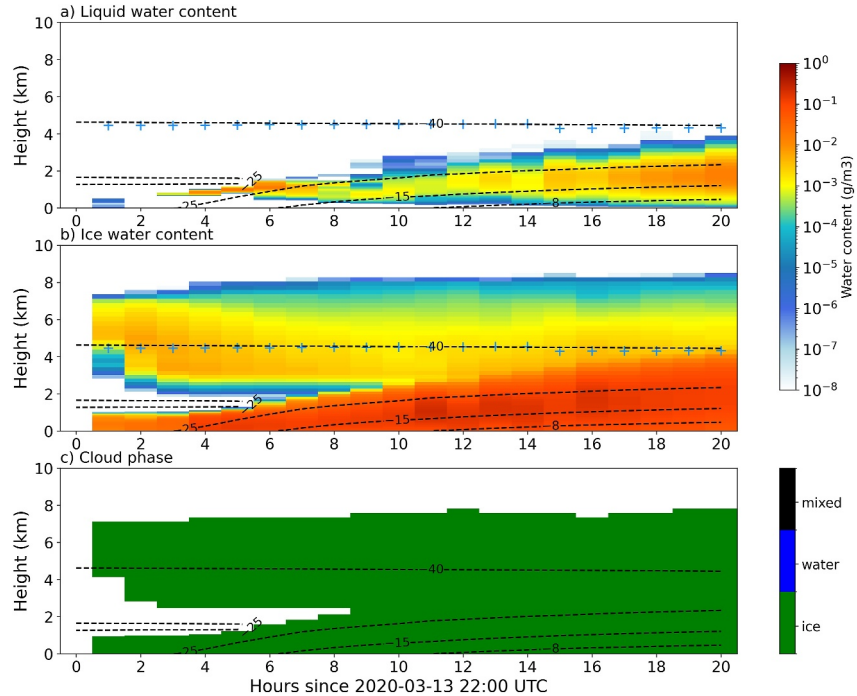

Figure 3. Temporal evolution of the domain-mean liquid water content (panel a), ice water content (panel b), and cloud phase (panel c) from the CTRL experiment. Isotherms are also shown in long-dashed black lines. Blue "+" symbols denote cloud top in the mixed-phase temperature ranges (see Section 5.2 and Figure 9 for details). Cloud phase is calculated as the ratio of liquid water content to the sum of liquid and ice water content. Ratio > 0.9: water; ratio < 0.1: ice; 0.1 < ratio < 0.9: mixed-phase.

Results from the experiment with this modification (CLDFRAC) show a notable improvement in the simulation of LWP throughout the entire simulation period (Figure 4).

This improvement is particularly important for grid cells where CF_i and CF_l differ substantially. The frequency of such grid cells–where CF_i exceeds CF_l–and the broader impacts of this code modification will be investigated in future studies using global SCREAM simulations.

5.1.2. Role of Deposition Ice Nucleation

Moreover, the timing and extent of ice formation governed by ice initiation processes determine the available surface area for vapor deposition, thereby depleting supercooled liquid water and influencing the liquid–ice phase balance. Whether SCREAM simulates the correct timing when the first ice appears and the appropriate abundance of ice crystals is investigated in this section.

Figure 8 shows the offline-calculated immersion freezing and deposition ice nucleation rates as a function of temperature, derived from three aerosol-aware ice nucleation parameterizations using observed aerosol size distributions collected at two sites during COMBLE as input. These calculations serve as observational references for comparison with the corresponding rates from DP-SCREAM simulations, highlighting the differences in ice formation efficiency between the aerosol-unaware parameterizations currently used in SCREAM and the aerosol-aware approaches. A detailed description of the offline calculations based on observed aerosol properties is provided in Appendix B.

The modeled immersion freezing rates span a wide range; for visualization clarity, only the 95th percentile values at each temperature bin are shown (top panels of Figure 8). At the Zeppelin Observatory site at 0 UTC, even the 95th percentile of the modeled immersion freezing rates is generally underestimated between 240 and 250 K when compared to the values of the three observation-derived parameterizations. Notably, the spread among the three observation-derived parameterizations is smaller than the discrepancy between the model and observations. For clouds further downstream at 18 UTC at the COMBLE site, the modeled immersion freezing rates at the 95th

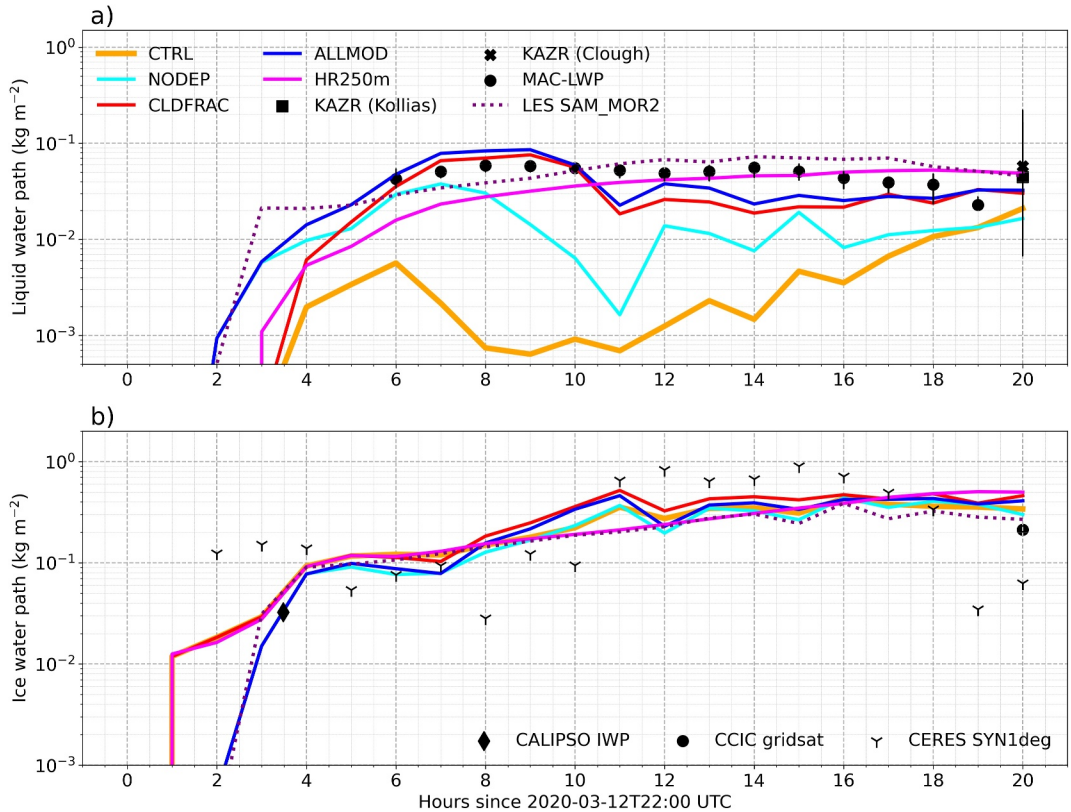

Figure 4. Temporal evolution of the domain-mean liquid water path (panel a) and ice water path (panel b) from model simulations and observations. The top and bottom of the error bars represent the 75th and 25th percentiles.

percentile align more closely with the observation-derived estimates (Figure 8), reinforcing the conclusion that the modeled immersion freezing rates are largely underestimated. However, the modeled deposition ice nucleation rates (Figure 8 middle panel) are significantly overestimated - by about one order of magnitude for upstream clouds and by about two orders of magnitude for downstream clouds in the lower temperature ranges, as compared to the values suggested by the ABIFM parameterization. When both nucleation modes are considered together (Figure 8 bottom panels), two key points emerge: (a) Deposition ice nucleation dominates total ice crystal production rates, especially under cold conditions; (b) The total nucleation rates are overestimated under colder conditions and underestimated under warmer conditions, with the discrepancy more pronounced in downstream clouds. As such, these results suggest that the simplified parameterizations used in SCREAM may misrepresent the true sensitivity of ice formation to aerosol properties, particularly in Arctic conditions where INP concentrations are both low and highly variable.

There is no doubt that the dominance of deposition ice nucleation in SCREAM would have a large impact on the Arctic mixed-phase cloud properties. To further investigate this impact, we conduct a sensitivity experiment in which deposition ice nucleation is deactivated (referred to as NODEP). This exclusion is supported by observational studies that found deposition and condensational freezing to be negligible for mixed-phase clouds (Ansmann et al., 2008; de Boer et al., 2011; Westbrook & Illingworth, 2011). As shown in Figure 4, the simulated LWP is increased to agree better with observations and LES results, particularly during the overcast cloud regime before 9 hr following 22 UTC on 12 March 2020. This improvement suggests that the low bias in supercooled liquid water may, in part, result from excessive ice crystal production, primarily driven by deposition ice nucleation (Figure 8). In contrast, when immersion freezing is deactivated, the simulated LWP shows minimal change compared to the default simulation (not shown), as expected. This outcome further confirms the dominant role of deposition ice nucleation in regulating ice production and, consequently, cloud phase partitioning in SCREAM.

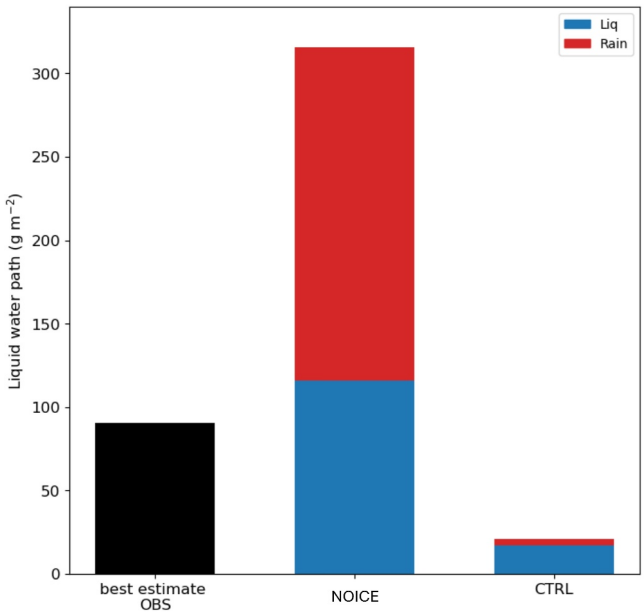

Figure 5. Comparison of liquid water paths (LWPs) between observation at the cold-air outbreaks in the marine boundary layer experiment ARM Mobile Facility site and DP-SCREAM simulations with the standard whole set of ice microphysics in P3 fully activated (CTRL) and fully deactivated (NOICE). Note that in the simulated LWP the rain was included (red) in addition to cloud liquid water (blue).

Examining the timing of the appearance of initial ice within mixed-phase clouds provides valuable insights into the ice nucleation parameterizations. As shown in Figure 4, in experiments where deposition ice nucleation is active (experiments CTRL, CLDFRAC, HR250 m), IWP with its lines from the three experiments being overlapping in the beginning appears about 2 hr earlier than the corresponding emergence of LWP. In contrast, in the set of experiments where deposition ice nucleation is deactivated, IWP and LWP emerge more simultaneously, typically about 2 hr into the simulation. Therefore, the active deposition ice nucleation explains the early onset of ice, which subsequently promotes depositional growth through water vapor (see Figure 6b: Vapor_deposition). Deposition ice nucleation is the only pathway in the model that does not involve liquid water, occurring instead by direct water vapor deposition onto a dry ice nucleus.

5.1.3. Role of All Modifications

Combining the two key modifications - improving the liquid-ice subgrid cloud overlap and deactivating the deposition ice nucleation parameterization (ALLMOD)–leads to a significantly improved simulation of LWP. The modeled LWP aligns well with both observations and LES results in terms of timing and magnitude throughout the entire simulation period (Figure 4). Specifically, turning off deposition ice nucleation corrects the premature onset of ice formation, while the refined treatment of subgrid cloud overlap enhances the overall LWP magnitude.

In summary, the pronounced underestimation of LWP in default SCREAM arises from a sequence of interrelated issues. The premature and excessive generation of ice crystals—primarily due to the deposition ice nucleation parameterization—leads to rapid ice growth via vapor deposition. This delays the onset of liquid condensation, resulting in ill-timed LWP and IWP evolution compared to LES benchmarks (Figure 4). Once liquid condensation does occur, the overly efficient WBF process quickly depletes the supercooled liquid, exacerbating the LWP bias. Together, these factors

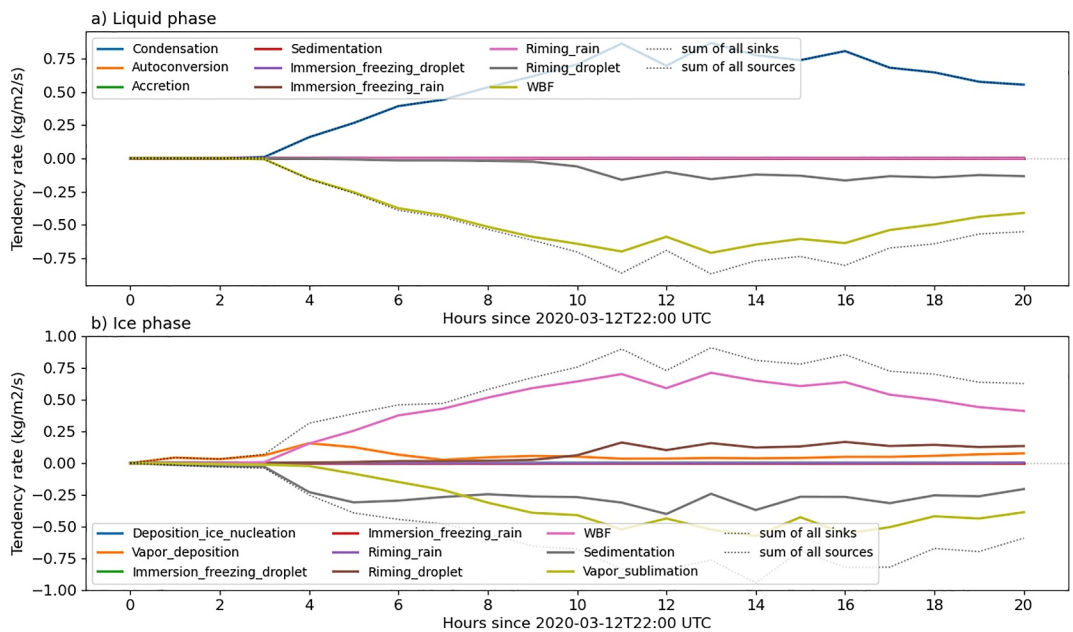

Figure 6. Time series of vertically integrated domain sum of sources (positive values) and sinks (negative values) for cloud liquid water (panel a) and ice (panel b) from the CTRL experiment.

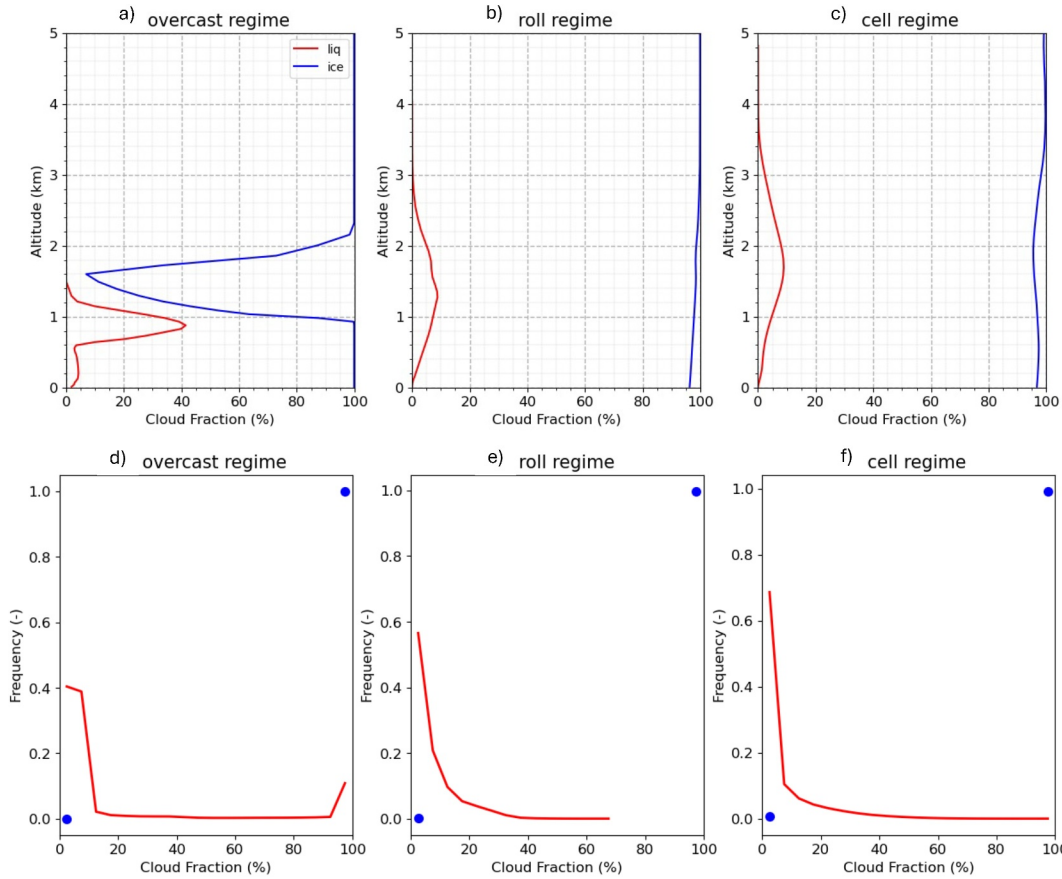

Figure 7. Top: domain-mean vertical profiles of liquid (red) and ice (blue) cloud fraction over the three different cloud regimes: overcast (a), roll (b) and cellular (c) structures. Bottom: Counted frequency (in fraction) of liquid (red) and ice (blue dot, 0 or 100) cloud fractions over different regimes (d–f).

highlight the critical role of both ice nucleation and cloud fraction representation in accurately simulating mixed-phase cloud processes.

5.1.4. Role of Model Horizontal Resolution

Increasing the model's horizontal resolution from 3 km to 250 m, while keeping other configurations unchanged (experiment HR250 m), leads to a notable improvement in the simulated LWP, bringing it into better agreement with observations and LES results (Figure 4). At finer horizontal grid spacing, the excessively strong WBF process rates caused primarily by the assumption of subgrid cloud overlap between liquid and ice cloud fractions are inherently mitigated. This improvement emerges because, at smaller grid scales, the difference between liquid and ice cloud fractions are reduced (see Figure S1 in Supporting Information S1), thereby lessening the impact of the erroneous subgrid cloud overlap assumption. Consequently, refining the model's grid resolution naturally alleviates the structural issue, enabling a more realistic simulation of mixed-phase cloud processes. Inhibiting the deposition ice nucleation parameterization at high resolution further improves the simulations of LWP in the overcast regime (not shown).

5.2. Cause and Impact of an Erroneous Ice Cloud Layer

While the physical formulations of parameterizations often receive more attention, the triggering functions that activate these parameterizations are equally critical. This section describes and examines the cause and impacts of an erroneous ice cloud layer that is falsely generated due to the highly uncertain triggering criteria within the deposition ice nucleation parameterization.

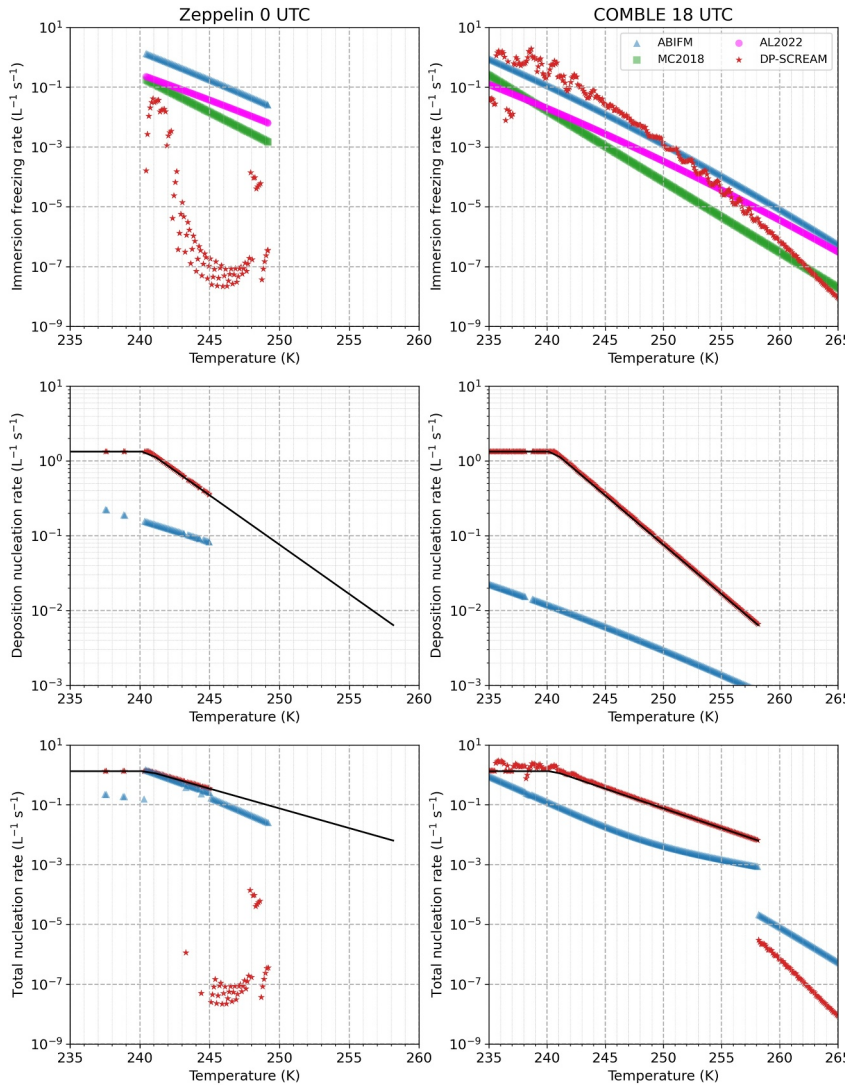

Figure 8. Comparison of ice nucleation rates from the immersion freezing mode (top), the deposition ice nucleation mode (middle) and the sum of the two (bottom) between DP-SCREAM model results (red stars) and the calculated values inferred from observed aerosol particle size distributions at the upstream Zeppelin (left) and downstream cold-air outbreaks in the marine boundary layer experiment (right) locations. Here, ABIFM (blue triangles) denotes the water-activity based immersion freezing and deposition ice nucleation mode of sea spray aerosol (Alpert et al., 2022). AL2022 (pink dots) denotes the singular ice nucleation active sites-based parameterization of sea spray aerosol (Alpert et al., 2022). MC2018 (green squares) denotes the singular ice nucleation active sites-based parameterization of sea spray aerosol (McCluskey et al., 2018). Black lines denote the deposition ice nucleation parameterization follows Cooper (1986) scheme. For clear visualization, modeled immersion freezing rates for a given temperature at the 95th percentile are shown.

Figure 9 illustrates the time series of domain-mean cloud top height and cloud top temperature. Both LES and CALIOP observation indicate that the upstream clouds off sea-ice edge are capped at about 1 km. As air masses move further downstream, these clouds gradually grow deep and have a cloud top reaching 4 km near the Norwegian coast (Figures 1b; Figure 9a), as indicated by LES, satellite and ground-based observations. LES simulates cloud tops for upstream and downstream clouds agreeing well with observations.

However, the default SCREAM (experiment CTRL) simulates a cloud top of about 4.5 km persistent throughout the whole simulation period, which deviates from observations. The time-height cross-section of ice water mixing ratios (Figure 3) shows that there is a layer of ice cloud hanging above the boundary layer clouds, with the lower portion of the ice cloud layer included in our search for the cloud top within the mixed-phase temperature ranges between 0°C and −40°C. The satellite radiance imagery from an infrared channel (11.45 μm) and the CALIPSO

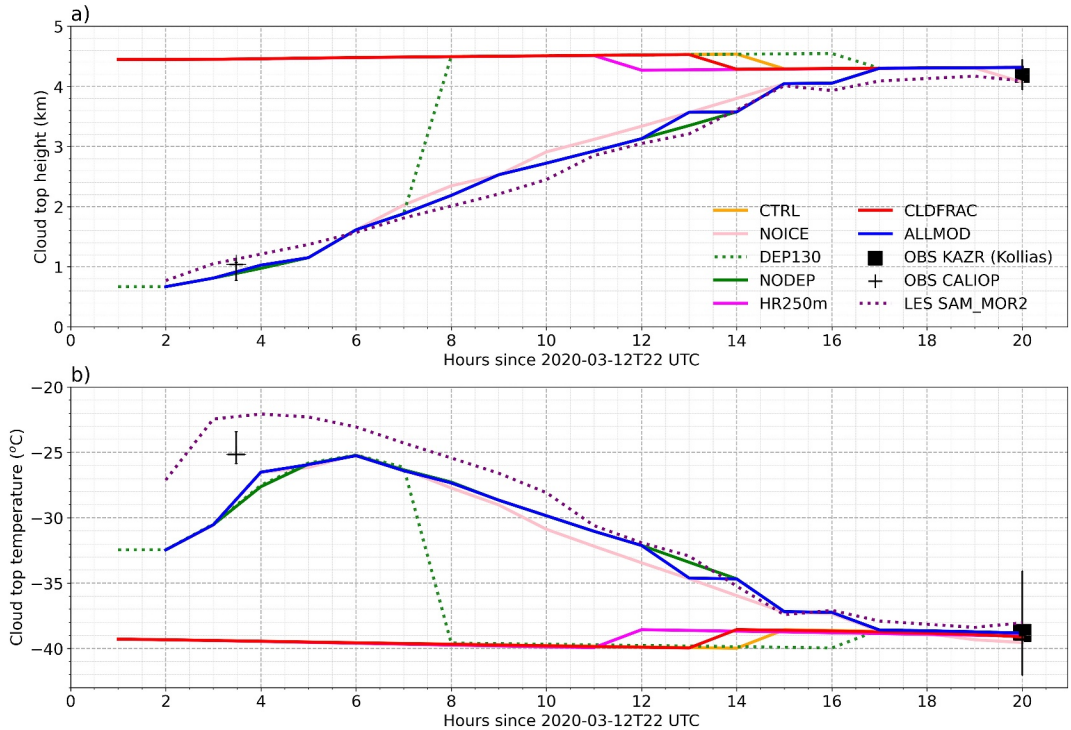

Figure 9. Temporal evolution of domain-mean cloud top height (panel a) and cloud top temperature (panel b) from observations and DP-SCREAM simulations. In DP-SCREAM runs, cloud top is determined specifically at the highest level where total cloud mixing ratio $(q_c + q_i) > 10^{-4}$ g kg^{-1} in the mixed-phase temperature ranges. The top and bottom of the error bars represent the 75th and 25th percentiles.

532 nm LiDAR backscatter signal (Figures 1a and 1b) which can detect thin ice clouds confirm that this ice cloud shield over the boundary layer clouds is absent. Tracing the causes, it is discovered that the deposition ice nucleation is responsible for the fictional ice cloud layer. Impeding the process of deposition ice nucleation by increasing the triggering ice supersaturation threshold from 105% to 130% prevents the erroneous ice cloud layer from occurring only before 7 hr since 2020-03-12 22 UTC (experiment DEP130 in Figure 9); the false ice cloud layer appears again for the rest of the simulation. Deactivating the deposition ice nucleation process (experiments NOICE, NODEP, ALLMOD) completely removes the false ice cloud layer and the evolution of cloud top height for the boundary layer clouds actually agrees well with LES and observations. Correcting the assumption of subgrid cloud overlap between liquid and ice clouds (CLDFRAC) has a limited impact on the simulated cloud top height. Increasing model horizontal resolution from the default 3 km to 250 m does not remove this erroneous high ice cloud as the deposition ice nucleation process is still triggered for the given temperature and humidity profiles, regardless of model horizontal resolution. The simulations of cloud top height and cloud top temperature are highly sensitive to the choices of the triggering criterion, suggesting that the triggering criterion of the deposition ice nucleation is highly uncertain.

Figure 10 shows the time series of model domain-mean outgoing longwave radiation (OLR) at the top-of-the-atmosphere (TOA) and cloud longwave radiative forcing (LWCF), compared to satellite observations. The OLR simulated by the default model (CTRL) is significantly underestimated, suggesting either excessive cloud coverage and/or cloud tops that are too cold (Figure 9). This discrepancy is primarily due to a cold ice cloud shield located above the boundary layer clouds and the warm ocean surface. These high, cold ice clouds emit less longwave radiation to space than is indicated by satellite observations. When deposition ice nucleation is deactivated—effectively removing the cold ice cloud shield—more OLR escapes to space, resulting in a much closer agreement with satellite data. This improvement also leads to a more realistic simulation of LWCF. The difference in OLR between simulations with and without the ice cloud shield is approximately 10 W m^{-2}, highlighting the substantial impact of this spurious ice cloud layer on the Arctic radiative energy budget. These

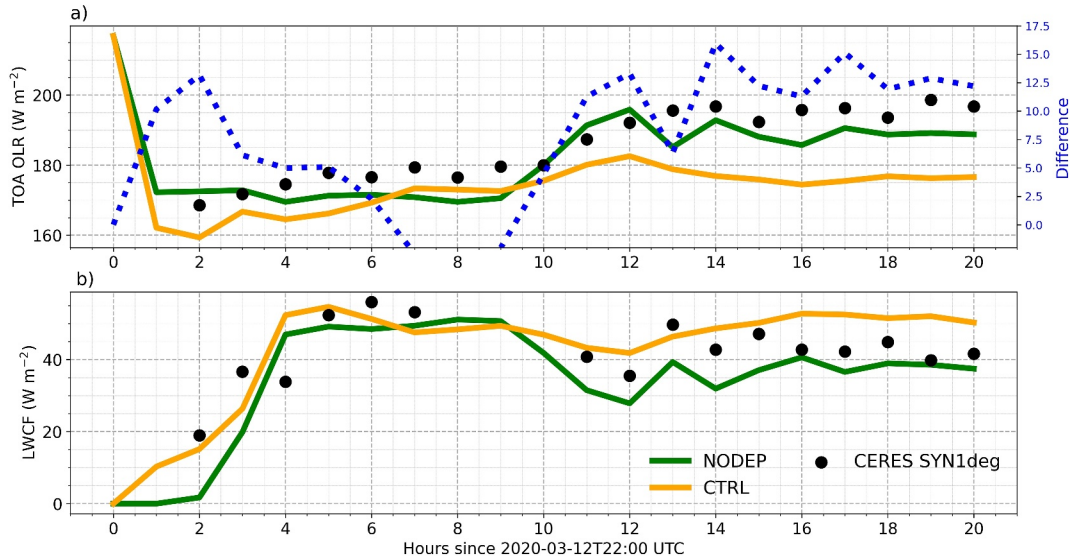

Figure 10. Temporal evolution of domain-mean top of the atmosphere (TOA) outgoing longwave radiation (OLR) and longwave cloud radiative forcing (LWCF) from model simulations (with and without the parameterization of deposition ice nucleation), as compared to observations. Differences in TOA OLR between the CTRL and NODEP simulations are also shown in panel a) in blue.

findings underscore the critical importance of accurately simulating cloud occurrence and properties to improve the fidelity of convection-permitting models.

5.3. Cloud-Top Liquid and Ice Phase Partitioning

In this section, we evaluate SCREAM's performance in simulating the liquid-ice phase partitioning and compare the results against CALIOP satellite observations. Figure 11 presents the simulated cloud-top supercooled liquid fraction (SLF) across different temperature bins, alongside observations from 13 March 2020 (Figure 1c) and a March climatology derived from 2019 to 2022. Because CALIOP retrievals are spatially and temporally sparse, direct comparisons along a single-day Lagrangian trajectory are not feasible. To partially address this limitation, we use the March 2019–2022 climatology of phase partitioning as a more robust observational baseline.

Satellite observations show a near-linear increase of SLFs with increasing cloud-top temperature below −25°C, followed by saturation above −20°C. The NOICE experiment, which yields 100% SLFs across all temperature ranges, serves as an upper-bound reference. SLFs from the control simulations (CTRL) are systematically underestimated relative to observations (Figure 11). Consistent with this finding, Zheng et al. (2024) reported that SCREAMv0 simulates too frequent glaciated ice clouds in cloud streets and scattered cumulus regimes with cloud-top temperature below −25°C, despite both satellite and ARM observations indicating a notable fraction of mixed-phase clouds.

The low bias in cloud-top SLFs in default SCREAM can be attributed largely to the overly strong WBF process, driven by an overabundance of ice crystals produced through deposition ice nucleation and by an inaccurate representation of subgrid cloud overlap between liquid and ice. Inhibition of the deposition ice nucleation parameterization (NODEP) notably increases SLFs, particularly for colder cloud-tops, bringing the results into closer agreement with satellite observations (Figure 11). This suggests that excessive ice crystals generated by active deposition ice nucleation strongly accelerate the conversion of supercooled liquid water to ice.

For warmer cloud tops, where deposition ice nucleation is inactive, the low SLF bias is primarily linked to the assumed subgrid overlap between liquid and ice. The sensitivity experiment with improved overlap treatment (CLDFRAC) shows a substantial SLF increase, aligning more closely with satellite observations that indicate near 100% SLFs for temperatures >−20°C. The exaggerated WBF process rates is largely responsible for the low bias in SLFs at these temperatures. When both modifications—disabling deposition ice nucleation and refining the cloud overlap assumption—are applied simultaneously in the ALLMOD experiment, SCREAM produces

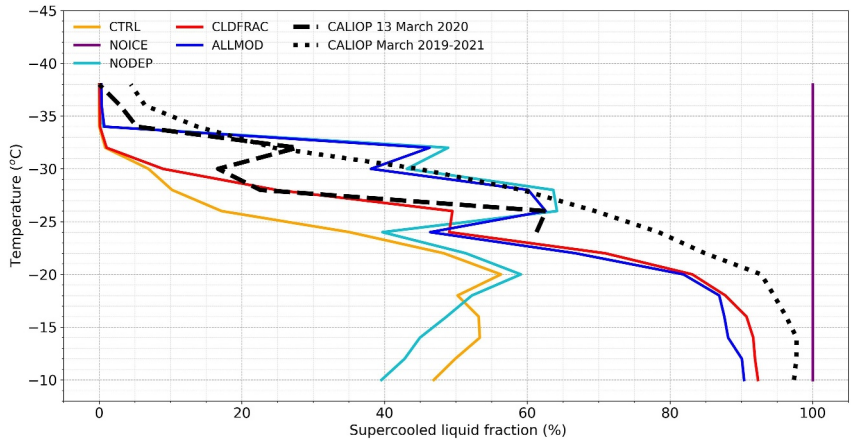

Figure 11. The supercooled liquid fraction (SLF) at cloud top for each temperature bin from model simulations and cloud-aerosol LiDAR with orthogonal polarization LiDAR. The black dashed line shows the SLF observed on 13 March 2020, along transects shown in Figure 1c while the black dotted line represents the March climatology from 2019 to 2021 over the Norwegian Sea bounded from 70°N to 75°N and 10°W to 15°E to obtain the more statistically robust results. Temperatures are binned into equal interval width of 2 from −10°C to −38°C.

more realistic SLFs across the full range of mixed-phase temperatures, demonstrating consistent improvements in phase partitioning fidelity.

6. Discussion

6.1. Generalization of Code Modification on Subgrid Cloud Overlap Treatment

The cold cloud-topped (<−25°C) convective cloud regime examined in this study exhibits a substantial bias, exposing the underlying structural deficiencies in the cloud parameterizations currently used in SCREAM. In contrast, the warm cloud-topped (>−15°C) stratocumulus cloud regime, such as the single-layer overcast mixed-phase clouds observed during M-PACE, does not show such a strong low bias in supercooled liquid water. In these cases, DP-SCREAM simulates a reasonable LWP as shown in Figure 10 of Bogenschutz et al. (2023). These deficiencies are less apparent in the warm stratiform cloud regime for several reasons discussed below.

First, overestimation of the WBF process rates is largely limited in near-overcast conditions, as suggested by the high liquid cloud fractions (see Figure S2 in Supporting Information S1). Comparable liquid and ice cloud fractions within a grid cell ameliorates the adverse effects of the assumption of subgrid cloud overlap. Second, for warm mixed-phase clouds, the triggering of deposition ice nucleation parameterization is substantially less frequent or even suppressed, limiting the over-production of ice crystals. This further suppresses the WBF process rate and in turn maintain supercooled liquid water.

Importantly, our proposed correction to the assumption of subgrid cloud overlap is broadly applicable across different cloud regimes. Implementing this correction does not degrade model performance in simulating warm cloud-topped stratiform mixed-phase clouds, but instead promotes more physically consistent behavior across a wider range of cloud conditions.

6.2. Should Deposition Ice Nucleation Be Dominant in Arctic Mixed-Phase Clouds?

Observational studies indicate that immersion freezing is the primary pathway for ice formation in high latitude mixed-phase clouds (Ansmann et al., 2008; de Boer et al., 2011; Westbrook & Illingworth, 2011) whereas deposition ice nucleation is considered negligible under these conditions (Ansmann et al., 2008; Kanji et al., 2017). Although the dominant ice-nucleation mode for 13 March 2020 cannot be firmly established due to limited observations, the strong dominance of deposition ice nucleation over immersion freezing simulated by SCREAM (Section 5.1.2; Figure 8) stands in contrast to the prevailing understanding of ice-nucleation processes in Arctic mixed-phase clouds.

Moreover, as ice particles typically originate from freezing of supercooled droplets, liquid water appears prior to or concurrently with ice (de Boer et al., 2011). Westbrook and Illingworth (2011) also report the negligence of deposition ice nucleation for producing first ice in clouds at temperature higher than −27°C. However, the parameterization of deposition ice nucleation in SCREAM now allows ice formation at temperatures as high as −15°C, leading to premature onset of ice before liquid appears. These weakly constrained triggering criteria could produce early ice generation and significant biases in cloud physical and radiative properties (Section 5.2), consistent with previous studies (e.g., Diao et al., 2017) showing that changing the triggering criteria yields wide variability in simulated cloud properties.

It should be noted that the deposition ice nucleation parameterization (Cooper, 1986) used in SCREAM is not specifically designed for representing the Arctic INPs which potentially degrades the realism of simulated mixed-phase cloud evolution. It predicts an INP concentration of 0.48 L^{-1} at −15°C (see Cooper parameterization in Section 2.1). This value far exceeds INP concentrations typically observed in the Arctic marine boundary layers, where dust-derived INPs are generally well below 0.01 L^{-1} (Irish et al., 2019; Welti et al., 2020). During the INPOP (Ice Nucleating Particles at Oliktok Point) field campaign that took place at a DOE ARM facility in the northern Alaskan Arctic in late May (Creamean et al., 2018), INP concentrations over open Arctic Ocean were observed at a maximum of 0.02 L^{-1} at −15°C. The highest recorded INP concentrations associated with Arctic haze in springtime cold-air outbreaks range from 0.18 to 2.1 L^{-1} (at −15°C), indicated from airborne measurements over the Norwegian and Barents seas as part of the March 2022 Arctic Cold-Air Outbreak (ACAO) field campaign (Raif et al., 2024). Ground-based measurements of INP concentrations from Andenes during COMBLE revealed INP concentrations that were 2–3 orders of magnitude lower than those in ACAO (Geerts et al., 2022). Therefore, the Cooper parameterization may substantially overpredicts INP abundance, especially in the cold Arctic, by predicting INP concentrations comparable to the Arctic highest recorded values (at −15°C).

Finally, the two ice nucleation parameterizations in SCREAM are a deterministic function of temperature and ignore the availability of atmospheric INPs–an important limitation in the Arctic, where INP sources and concentrations are highly variable (Raif et al., 2024). In contrast, the three observation-driven ice nucleation parameterizations applied in this study capture lower downstream INP concentrations (Figure 8) due to aerosol precipitation scavenging during air mass transport (Williams et al., 2024). Modeling with a dynamic aerosol budget shows rapid exhaust of the deposition ice nuclei due to precipitation scavenging, indicating that deposition nucleation cannot be sustained (Morrison, Shupe, et al., 2005). However, aerosol-unaware parameterizations fail to capture these changes in the aerosol budget and omit many physical processes, limiting the realism and accuracy of ice formation predictions.

7. Summary, Conclusions and Outlook

Using a doubly periodic configuration, we evaluate the DOE's GCPM, SCREAM, at its native 3.25-km grid spacing for Arctic mixed-phase cloud simulations. The assessment is based on a cold-air outbreak case over the Norwegian Sea, compared against LES, satellite retrievals, and COMBLE ground-based observations. SCREAM captures the mesoscale transitions between distinct cloud regimes (Zheng et al., 2024), but shows a persistent low bias in supercooled liquid water within cold convective mixed-phase clouds, largely due to uncertainties in ice microphysical processes. This bias is much smaller in warm stratiform regimes.

The low bias in supercooled liquid arises from two factors: (a) the erroneous subgrid cloud overlap between liquid and ice cloud fractions, which notoriously amplifies the WBF process, and (b) excessive ice crystal production from an uncertain deposition ice nucleation parameterization. Improving the overlap assumption and disabling deposition ice nucleation both improve agreement with observations. Moreover, increasing horizontal resolution (e.g., to 250 m) naturally reduces liquid-ice cloud fraction disparity, thereby alleviating the overestimation of the WBF process, but it does not eliminate the spurious ice clouds, as the deposition ice nucleation parameterization remains insensitive to resolution. These findings highlight that parameterizations of subgrid-scale processes, particularly cloud microphysics, continue to be a major source of uncertainty in convection-permitting models.

Many previous studies (e.g., Tan et al., 2016; Zelinka et al., 2020) have emphasized that a realistic representation of present-day SLF in mixed-phase clouds is critical for constraining cloud-phase feedbacks in a warming

climate. The feedback strength is largely controlled by the extent to which cloud phase transitions in response to warming. The default SCREAM tends to underestimate SLFs, potentially producing an overly strong cloud phase feedback and, consequently, underestimating future global warming. Therefore, to use SCREAM effectively for weather and climate analysis, it is essential to improve the representation of SLFs in mixed-phase clouds by accounting for the key physical processes that govern cloud phase partitioning, such as incorporating the modifications proposed in this study. SCREAMv0, written in Fortran 90, serves as the scientific foundation for SCREAMv1, a faster C++ GPU-enabled version. Since both are scientifically equivalent, our findings and proposed corrections in SCREAMv0 directly inform SCREAMv1 development.

As global kilometer-scale modeling advances, the foremost priority is optimizing computational performance so models can meet stringent throughput targets. Achieving this speed, however, comes with trade-offs: high resolution often requires simplified treatments of subgrid processes, especially cloud microphysics. Consequently, these models show substantial spread in simulated microphysical properties and radiative effects (Atlas et al., 2024; Turbeville et al., 2022), and sometimes perform worse than lower-resolution systems. Balancing computational efficiency and physical accuracy remains a key challenge in advancing next-generation kilometer-scale modeling. A promising path forward is to strategically replace traditional costly parameterizations with data-driven, high-efficiency schemes (e.g., Lamb et al., 2024; Seifert & Siewert, 2024) enabling more detailed cloud microphysics without compromising computational speed—adding values to the success achieved by fine model grid spacing.

Appendix A: Description of Data Sets

Table A1
Summary of Reference Data Sets

Product	Description	Variable	Resolution	Uncertainty
VNP02IMG	Visible Infrared Imaging Radiometer Suite (VIIRS) Level-1B calibrated radiances product (Cao et al., 2013)	I05 band radiance		
MAC-LWP	Multisensor Advanced Climatology of Liquid Water Path (Elsaesser et al., 2017)	Liquid water path	0.25° over ocean	20%
2C-ICE	CloudSat-CALIPSO Level-2C Ice Cloud Property Product (Deng et al., 2010, 2013, 2015)	Ice water path	1 km along track	30%
CERES_SYN1deg-1Hour_Ed4A	NASA Clouds and the Earth's Radiant Energy System (CERES) synoptic (SYN) cloud and radiation level 3 data products (https://ceres.larc.nasa.gov/data/#synoptic-toa-and-surface-fluxes-and-clouds-syn)	Ice water path, TOA radiative fluxes	1° × 1°, hourly	
CCIC	The Chalmers Cloud Ice Climatology (CCIC) ice cloud property data set (Amell et al., 2024; Pfreundschuh et al., 2025)	Ice water path	0.036°, 30 min	Inherents bias from 2C-ICE
CAL_LID_L2_01kmCLay	CALIPSO LiDAR Level 2 1 km Cloud Layer data product	Liquid and ice phase flags; cloud top height and temperature	Horizontal: 1 km; vertical: 30 m	
30qcecor	Quality-Controlled Eddy Correlation Flux Measurement value-added product (QCECOR VAP). Data stream: anx30qcecorM1.c1. (https://doi.org/10.5439/1097546)	Surface heat fluxes		
MWRRET1LILJCLOU	Microwave Radiometer Retrieval (MWRRET) (Liljegren et al., 2001). Data stream: anxmwrret1liljclouM1.c2. (https://doi.org/10.5439/1285691)	Liquid water path		20 g m^{-2} for LWP < 200 g m^{-2}

Table A1
Continued

Product	Description	Variable	Resolution	Uncertainty
ARSCLKAZRBND1KOLLIAS	Cloud boundaries retrieved from KAZRARSCL: first Kollias algorithm. Data stream: anxarsclkazrbnd1kolliasM1.c1. (https://doi.org/10.5439/1228769)	Cloud top height and temperature	30 m, 4 s	30 m
LES_SAM_MOR2	LES simulations of the same CAO case serve as numerical benchmark	Surface heat fluxes, liquid water path, ice water path, cloud top height, cloud top temperature		

Appendix B: Description of Ice Nucleation Rates Inferred From Observed Aerosol Size Distribution and SCREAM

The Sun and Knopf aerosol-INP closure study for the 13 March 2020 MCAO event (https://arm-development.github.io/comble-mip/notebooks/setup/aerosol-inp-closure.html) estimates immersion-mode INP concentrations under the assumption that all aerosol particles are sea spray. Ambient aerosol particle size distributions (PSDs) measured at the Zeppelin Observatory at Svalbard (approximately 1,000 km upwind from Andenes) at 00 UTC and at the AMF site (downwind) at 18 UTC 13 March 2020 are used as input to a simplistic 1D aerosol-cloud model (Knopf et al., 2023, code is available at https://github.com/open-atmos/AC-1D). Post-processed PSD parameters including number concentration, mode radius, standard deviation of multiple log-normal modes are provided at https://arm-development.github.io/comble-mip/notebooks/setup/aerosol-inp-closure.html. Their study evaluates two deterministic immersion freezing parameterizations - both based on the singular ice-active-site framework for sea spray aerosol (MC2018: McCluskey et al. (2018); AL2022: Alpert et al. (2022))–and one stochastic water activity-based immersion freezing scheme (ABIFM) (Alpert et al., 2022). The resulting immersion-mode INP concentrations are directly mapped to ice crystal number concentrations and compared with the values produced by DP-SCREAM's immersion freezing parameterization.

In this study, we extend their approach by computing deposition-mode INP concentrations for sea spray aerosols using the ABIFM method (Alpert et al., 2022). Sea spray aerosol, produced mainly by bubble bursting and wave breaking, is closely tied to surface wind speed during the COMBLE campaign (Williams et al., 2024). For the 13 March 2020 MCAO case, the air mass spent the preceding 20 hr over open ocean and arrived at Andenes under strong, sustained northwesterly winds (Figure 1a; Figure 2 in Geerts et al., 2022). Thus, sea spray aerosol is likely an important INP source during this period, with potential impacts on key cloud processes. Because aerosol composition measurements are unavailable, we assume sea spray aerosol dominates the ambient aerosol population, consistent with the Sun and Knopf aerosol–INP closure study.

SCREAM employs two temperature-dependent heterogeneous ice nucleation parameterizations (see Section 2.1.2) that directly map diagnosed INPs to ice crystal number concentrations. Direct observations of ice crystal numbers were not available during COMBLE, and SCREAM does not carry prognostic INP information to reduce computational cost. On the other hand, the aerosol-INP closure study (https://arm-development.github.io/comble-mip/notebooks/setup/aerosol-inp-closure.html) can only estimate INP concentrations observed ambient aerosol PSDs. Despite these limitations and the mismatch between modeled and observed quantities, we qualitatively assess SCREAM's ice nucleation processes using observations, motivated by our results and prior work (e.g., Morrison, Shupe, et al., 2005) showing that ice nucleation strongly regulates supercooled liquid in mixed-phase clouds.

To do so, we compare modeled immersion freezing and deposition nucleation rates - fundamental quantities for ice formation - with rates derived from aerosol-aware parameterizations driven by observed PSDs and model temperature. SCREAM directly diagnoses the immersion freezing rate (Section 2.1.2). For deposition ice nucleation, its parameterization outputs ice crystal number concentrations, from which we infer the nucleation rate by dividing by the model timestep (i.e., 75 s, Section 3). Observationally derived immersion freezing and deposition nucleation rates are computed in the same way, using the calculated INP concentrations and the same timestep.

Conflict of Interest

The authors declare no conflicts of interest relevant to this study.

Data Availability Statement

The Simple Cloud-Resolving E3SM Atmosphere model is an open-source model and the model code is publicly available at https://github.com/E3SM-Project/E3SM. The run script for the COMBLE case can be found at https://github.com/E3SM-Project/scmlib. The MAC-LWP data set is currently hosted at the Goddard Earth Sciences Data and Information Services Center. CERES SYN1deg Ed4A is download at https://ceres.larc.nasa.gov/data/#synoptic-toa459-and-surface-fluxes-and-clouds-syn. Ground-based observations during COMBLE field campaign can be accessed and downloaded from DOE ARM's Data Discovery at https://adc.arm.gov/discovery/#/ with a free ARM user account profile. Back trajectories for identified cold-air outbreak cases from the Cold-Air Outbreaks in the Marine Boundary Layer Experiment (COMBLE) (https://doi.org/10.5439/1843763) are available at the ARM Data Center (https://www.arm.gov/news/data/post/78207). ARSCLKAZRBND1KOLLIAS (DOI: 10.5439/1228769) provides estimates of cloud top height and liquid water path. ARSCLKAZRBND1-KOLLIAS can be downloaded at https://adc.arm.gov/discovery/#/results/meas_category_code::cloud%2FiopShortName::amf2019comble. The model output data sets are available at Lin (2025) https://zenodo.org/records/15724269.

Acknowledgments

This work was mainly supported by the DOE Office of Science Atmospheric System Research (ASR) Tying in High Resolution E3SM with ARM Data (THREAD) project. P. Wu acknowledges support from the DOE ASR ICLASS project. This work was performed under the auspices of the U.S. Department of Energy by Lawrence Livermore National Laboratory under contract DE-AC52-07NA27344. Lawrence Livermore National Security, LLC. PNNL is operated for the Department of Energy by Battelle Memorial Institute under Contract DE-AC05-76 RL01830. The authors acknowledge high-performance computing support from the Perlmutter supercomputer at the National Energy Research Scientific Computing Center at Lawrence Berkeley National Laboratory. The authors also thank HDF-EOS Tools and Information Center (https://www.hdfeos.org/index.php) for providing programming examples in Python for various NASA HDF/HDF-EOS data products.

References

Abel, S. J., Boutle, I. A., Waite, K., Fox, S., Brown, P. R. A., Cotton, R., et al. (2017). The role of precipitation in controlling the transition from stratocumulus to cumulus clouds in a northern hemisphere cold-air outbreak. *Journal of the Atmospheric Sciences*, *74*(7), 2293–2314. https://doi.org/10.1175/JAS-D-16-0362.1

Alpert, P. A., Kilthau, W. P., O'Brien, R. E., Moffet, R. C., Gilles, M. K., Wang, B., et al. (2022). Ice-nucleating agents in sea spray aerosol identified and quantified with a holistic multimodal freezing model. *Science Advances*, *8*(44), eabq6842. https://doi.org/10.1126/sciadv.abq6842

Amell, A., Pfreundschuh, S., & Eriksson, P. (2024). The chalmers cloud ice climatology: Retrieval implementation and validation. *Atmospheric Measurement Techniques*, *17*(14), 4337–4368. https://doi.org/10.5194/amt-17-4337-2024

Ansmann, A., Tesche, M., Althausen, D., Müller, D., Seifert, P., Freudenthaler, V., et al. (2008). Influence of saharan dust on cloud glaciation in southern Morocco during the saharan mineral dust experiment. *Journal of Geophysical Research*, *113*(D4). https://doi.org/10.1029/2007JD008785

Atlas, R. L., Bretherton, C. S., Sokol, A. B., Blossey, P. N., & Khairoutdinov, M. F. (2024). Tropical cirrus are highly sensitive to ice microphysics within a nudged global storm-resolving model. *Geophysical Research Letters*, *51*(1), e2023GL105868. https://doi.org/10.1029/2023GL105868

Barrett, A. I., Hogan, R. J., & Forbes, R. M. (2017). Why are mixed-phase altocumulus clouds poorly predicted by large-scale models? Part 1. physical processes. *Journal of Geophysical Research: Atmospheres*, *122*(18), 9903–9926. https://doi.org/10.1002/2016JD026321

Bigg, E. K. (1953). The formation of atmospheric ice crystals by the freezing of droplets. *Quarterly Journal of the Royal Meteorological Society*, *79*(342), 510–519. https://doi.org/10.1002/qj.49707934207

Bogenschutz, P. A., Clevenger, T. C., Bradley, A., Caldwell, P. M., Beydoun, H., Mahfouz, N., et al. (2025). High performance, high fidelity: A gpu-accelerated doubly-periodic version of the simple cloud-resolving e3sm atmosphere model version 1 (dp-screamv1). *ESS Open Archive*. https://doi.org/10.22541/essoar.174534217.73452258/v1

Bogenschutz, P. A., Eldred, C., & Caldwell, P. M. (2023). Horizontal resolution sensitivity of the simple convection-permitting e3sm atmosphere model in a doubly-periodic configuration. *Journal of Advances in Modeling Earth Systems*, *15*(7), e2022MS003466. https://doi.org/10.1029/2022MS003466

Bogenschutz, P. A., & Krueger, S. K. (2013). A simplified pdf parameterization of subgrid-scale clouds and turbulence for cloud-resolving models. *Journal of Advances in Modeling Earth Systems*, *5*(2), 195–211. https://doi.org/10.1002/jame.20018

Bogenschutz, P. A., Zhang, Y., Zheng, X., Tian, Y., Zhang, M., Lin, L., et al. (2025). Exposing process-level biases in a global cloud permitting model with ARM observations. *Journal of Geophysical Research: Atmospheres*, *130*(12), e2024JD043059. https://doi.org/10.1029/2024jd043059

Brümmer, B. (1999). Roll and cell convection in wintertime arctic cold-air outbreaks. *Journal of the Atmospheric Sciences*, *56*(15), 2613–2636. https://doi.org/10.1175/1520-0469(1999)056<2613:racciw>2.0.co;2

Caldwell, P. M., Terai, C. R., Hillman, B., Keen, N. D., Bogenschutz, P., Lin, W., et al. (2021). Convection-permitting simulations with the e3sm global atmosphere model. *Journal of Advances in Modeling Earth Systems*, *13*(11), e2021MS002544. https://doi.org/10.1029/2021MS002544

Cao, C., Xiong, J., Blonski, S., Liu, Q., Uprety, S., Shao, X., et al. (2013). Suomi npp viirs sensor data record verification, validation, and long-term performance monitoring. *Journal of Geophysical Research: Atmospheres*, *118*(20), 11664–11678. https://doi.org/10.1002/2013JD020418

Cooper, W. A. (1986). Ice initiation in natural clouds. *Meteorological Monographs*, *21*(43), 29–32. https://doi.org/10.1175/0065-9401-21.43.29

Coopman, Q., & Tan, I. (2023). Characterization of the spatial distribution of the thermodynamic phase within mixed-phase clouds using satellite observations. *Geophysical Research Letters*, *50*(24), e2023GL104977. https://doi.org/10.1029/2023GL104977

Creamean, J. M., Kirpes, R. M., Pratt, K. A., Spada, N. J., Maahn, M., de Boer, G., et al. (2018). Marine and terrestrial influences on ice nucleating particles during continuous springtime measurements in an arctic oilfield location. *Atmospheric Chemistry and Physics*, *18*(24), 18023–18042. https://doi.org/10.5194/acp-18-18023-2018

D'Alessandro, J. J., McFarquhar, G. M., Wu, W., Stith, J. L., Jensen, J. B., & Rauber, R. M. (2021). Characterizing the occurrence and spatial heterogeneity of liquid, ice, and mixed phase low-level clouds over the southern ocean using in situ observations acquired during socrates. *Journal of Geophysical Research: Atmospheres*, *126*(11), e2020JD034482. https://doi.org/10.1029/2020JD034482

de Boer, G., Morrison, H., Shupe, M. D., & Hildner, R. (2011). Evidence of liquid dependent ice nucleation in high-latitude stratiform clouds from surface remote sensors. *Geophysical Research Letters*, *38*(1). https://doi.org/10.1029/2010GL046016

Deng, M., Mace, G. G., Wang, Z., & Berry, E. (2015). Cloudsat 2c-ice product update with a new ze parameterization in LiDAR-only region. *Journal of Geophysical Research: Atmospheres*, *120*(23), 12198–12208. https://doi.org/10.1002/2015JD023600

Deng, M., Mace, G. G., Wang, Z., & Lawson, R. P. (2013). Evaluation of several a-train ice cloud retrieval products with in situ measurements collected during the sparticus campaign. *Journal of Applied Meteorology and Climatology*, *52*(4), 1014–1030. https://doi.org/10.1175/JAMC-D-12-054.1

Deng, M., Mace, G. G., Wang, Z., & Okamoto, H. (2010). Tropical composition, cloud and climate coupling experiment validation for cirrus cloud profiling retrieval using cloudsat radar and calipso lidar. *Journal of Geophysical Research*, *115*(D10). https://doi.org/10.1029/2009JD013104

Diao, M., Bryan, G. H., Morrison, H., & Jensen, J. B. (2017). Ice nucleation parameterization and relative humidity distribution in idealized squall-line simulations. *Journal of the Atmospheric Sciences*, *74*(9), 2761–2787. https://doi.org/10.1175/JAS-D-16-0356.1

Donahue, A. S., Caldwell, P. M., Bertagna, L., Beydoun, H., Bogenschutz, P. A., Bradley, A. M., et al. (2024). To exascale and beyond—the simple cloud-resolving e3sm atmosphere model (scream), a performance portable global atmosphere model for cloud-resolving scales. *Journal of Advances in Modeling Earth Systems*, *16*(7), e2024MS004314. https://doi.org/10.1029/2024MS004314

Elsaesser, G. S., O'Dell, C. W., Lebsock, M. D., Bennartz, R., Greenwald, T. J., & Wentz, F. J. (2017). The multisensor advanced climatology of liquid water path (Mac-lwp). *Journal of Climate*, *30*(24), 10193–10210. https://doi.org/10.1175/JCLI-D-16-0902.1

Evans, M. D., Abel, S. J., Field, P. R., Finney, D. L., Lloyd, G., Cotton, R. J., et al. (2025). Characterising the spatial overlap between liquid and ice in mixed-phase clouds. *Quarterly Journal of the Royal Meteorological Society, n/a(n/a)*, *151*(772), e5041. https://doi.org/10.1002/qj.5041

Fletcher, J., Mason, S., & Jakob, C. (2016a). The climatology, meteorology, and boundary layer structure of marine cold air outbreaks in both hemispheres. *Journal of Climate*, *29*(6), 1999–2014. https://doi.org/10.1175/jcli-d-15-0268.1

Fletcher, J. K., Mason, S., & Jakob, C. (2016b). A climatology of clouds in marine cold air outbreaks in both hemispheres. *Journal of Climate*, *29*(18), 6677–6692. https://doi.org/10.1175/JCLI-D-15-0783.1

Geerts, B., Giangrande, S. E., McFarquhar, G. M., Xue, L., Abel, S. J., Comstock, J. M., et al. (2022). The comble campaign: A study of marine boundary layer clouds in arctic cold-air outbreaks. *Bulletin America Meteorology Social*, *103*(5), E1371–E1389. https://doi.org/10.1175/BAMS-D-21-0044.1

Gettelman, A., Liu, X., Ghan, S. J., Morrison, H., Park, S., Conley, A. J., et al. (2010). Global simulations of ice nucleation and ice supersaturation with an improved cloud scheme in the community atmosphere model. *Journal of Geophysical Research*, *115*(D18). https://doi.org/10.1029/2009JD013797

Gjelsvik, A. B., David, R. O., Carlsen, T., Hellmuth, F., Hofer, S., McGraw, Z., et al. (2024). Using a region-specific ice-nucleating particle parameterization improves the representation of arctic clouds in a global climate model. *EGUsphere*, *2024*, 1–32. https://doi.org/10.5194/egusphere-2024-1879

Hersbach, H., Bell, B., Berrisford, P., Hirahara, S., Horányi, A., Muñoz-Sabater, J., et al. (2020). The ERA5 global reanalysis. *Quarterly Journal of the Royal Meteorological Society*, *146*(730), 1999–2049. https://doi.org/10.1002/qj.3803

Irish, V. E., Hanna, S. J., Willis, M. D., China, S., Thomas, J. L., Wentzell, J. J. B., et al. (2019). Ice nucleating particles in the marine boundary layer in the canadian arctic during summer 2014. *Atmospheric Chemistry and Physics*, *19*(2), 1027–1039. https://doi.org/10.5194/acp-19-1027-2019

Kanji, Z. A., Ladino, L. A., Wex, H., Boose, Y., Burkert-Kohn, M., Cziczo, D. J., & Krämer, M. (2017). Overview of ice nucleating particles. *Meteorological Monographs*, *58*, 1.1–1.33. https://doi.org/10.1175/AMSMONOGRAPHS-D-16-0006.1

Khairoutdinov, M. F., & Randall, D. A. (2003). Cloud resolving modeling of the arm summer 1997 iop: Model formulation, results, uncertainties, and sensitivities. *Journal of the Atmospheric Sciences*, *60*(4), 607–625. https://doi.org/10.1175/1520-0469(2003)060⟨0607:CRMOTA⟩2.0.CO;2

Klein, S. A., McCoy, R. B., Morrison, H., Ackerman, A. S., Avramov, A., Boer, G. d., et al. (2009). Intercomparison of model simulations of mixed-phase clouds observed during the arm mixed-phase arctic cloud experiment. i: Single-layer cloud. *Quarterly Journal of the Royal Meteorological Society*, *135*(641), 979–1002. https://doi.org/10.1002/qj.416

Knopf, D. A., Silber, I., Riemer, N., Fridlind, A. M., & Ackerman, A. S. (2023). A 1d model for nucleation of ice from aerosol particles: An application to a mixed-phase arctic stratus cloud layer. *Journal of Advances in Modeling Earth Systems*, *15*(10), e2023MS003663. https://doi.org/10.1029/2023MS003663

Komurcu, M., Storelvmo, T., Tan, I., Lohmann, U., Yun, Y., Penner, J. E., et al. (2014). Intercomparison of the cloud water phase among global climate models. *Journal of Geophysical Research: Atmospheres*, *119*(6), 3372–3400. https://doi.org/10.1002/2013JD021119

Korolev, A., & Milbrandt, J. (2022). How are mixed-phase clouds mixed? *Geophysical Research Letters*, *49*(18), e2022GL099578. https://doi.org/10.1029/2022GL099578

Lackner, C. P., Geerts, B., Juliano, T. W., Xue, L., & Kosovic, B. (2023). Vertical structure of clouds and precipitation during arctic cold-air outbreaks and warm-air intrusions: Observations from comble. *Journal of Geophysical Research: Atmospheres*, *128*(13), e2022JD038403. https://doi.org/10.1029/2022JD038403

Lamb, K. D., van Lier-Walqui, M., Santos, S., & Morrison, H. (2024). Reduced-order modeling for linearized representations of microphysical process rates. *Journal of Advances in Modeling Earth Systems*, *16*(7), e2023MS003918. https://doi.org/10.1029/2023MS003918

Liljegren, J. C., Clothiaux, E. E., Mace, G. G., Kato, S., & Dong, X. (2001). A new retrieval for cloud liquid water path using a ground-based microwave radiometer and measurements of cloud temperature. *Journal of Geophysical Research*, *106*(D13), 14485–14500. https://doi.org/10.1029/2000JD900817

Lin, L. (2025). Simulation output for manuscript improving simulation of mixed-phase clouds in the convection-permitting e3sm atmosphere model: Lessons from an arctic cold-air outbreak. *Zenodo*. https://doi.org/10.5281/zenodo.15724269

Mages, Z., Kollias, P., Zhu, Z., & Luke, E. P. (2023). Surface-based observations of cold-air outbreak clouds during the comble field campaign. *Atmospheric Chemistry and Physics*, *23*(6), 3561–3574. https://doi.org/10.5194/acp-23-3561-2023

McCluskey, C. S., Ovadnevaite, J., Rinaldi, M., Atkinson, J., Belosi, F., Ceburnis, D., et al. (2018). Marine and terrestrial organic ice-nucleating particles in pristine marine to continentally influenced northeast atlantic air masses. *Journal of Geophysical Research: Atmospheres*, *123*(11), 6196–6212. https://doi.org/10.1029/2017JD028033

Meyers, M. P., DeMott, P. J., & Cotton, W. R. (1992). New primary ice-nucleation parameterizations in an explicit cloud model. *Journal of Applied Meteorology and Climatology*, *31*(7), 708–721. https://doi.org/10.1175/1520-0450(1992)031⟨0708:NPINPI⟩2.0.CO;2

Morrison, H., Curry, J. A., & Khvorostyanov, V. I. (2005a). A new double-moment microphysics parameterization for application in cloud and climate models. part i: Description. *Journal of the Atmospheric Sciences*, *62*(6), 1665–1677. https://doi.org/10.1175/JAS3446.1

Morrison, H., & Gettelman, A. (2008). A new two-moment bulk stratiform cloud microphysics scheme in the community atmosphere model, version 3 (cam3). part i: Description and numerical tests. *Journal of Climate*, *21*(15), 3642–3659. https://doi.org/10.1175/2008JCLI2105.1

Morrison, H., & Milbrandt, J. A. (2015). Parameterization of cloud microphysics based on the prediction of bulk ice particle properties. part i: Scheme description and idealized tests. *Journal of the Atmospheric Sciences*, *72*(1), 287–311. https://doi.org/10.1175/JAS-D-14-0065.1

Morrison, H., Shupe, M. D., Pinto, J. O., & Curry, J. A. (2005b). Possible roles of ice nucleation mode and ice nuclei depletion in the extended lifetime of arctic mixed-phase clouds. *Geophysical Research Letters*, *32*(18). https://doi.org/10.1029/2005GL023614

Ovchinnikov, M., Ackerman, A. S., Avramov, A., Cheng, A., Fan, J., Fridlind, A. M., et al. (2014). Intercomparison of large-eddy simulations of arctic mixed-phase clouds: Importance of ice size distribution assumptions. *Journal of Advances in Modeling Earth Systems*, *6*(1), 223–248. https://doi.org/10.1002/2013MS000282

Pfreundschuh, S., Kukulies, J., Amell, A., Hallborn, H., May, E., & Eriksson, P. (2025). The chalmers cloud ice climatology: A novel robust climate record of frozen cloud hydrometeor concentrations. *Journal of Geophysical Research: Atmospheres*, *130*(6), e2024JD042618. https://doi.org/10.1029/2024JD042618

Pithan, F., Medeiros, B., & Mauritsen, T. (2014). Mixed-phase clouds cause climate model biases in arctic wintertime temperature inversions. *Climate Dynamics*, *43*(1–2), 289–303. https://doi.org/10.1007/s00382-013-1964-9

Pithan, F., Svensson, G., Caballero, R., Chechin, D., Cronin, T. W., Ekman, A. M. L., et al. (2018). Role of air-mass transformations in exchange between the arctic and mid-latitudes. *Nature Geoscience*, *11*, 805–812. https://doi.org/10.1038/s41561-018-0234-1

Raatikainen, T., Prank, M., Ahola, J., Kokkola, H., Tonttila, J., & Romakkaniemi, S. (2022). The effect of marine ice-nucleating particles on mixed-phase clouds. *Atmospheric Chemistry and Physics*, *22*(6), 3763–3778. https://doi.org/10.5194/acp-22-3763-2022

Raif, E. N., Barr, S. L., Tarn, M. D., McQuaid, J. B., Daily, M. I., Abel, S. J., et al. (2024). High ice-nucleating particle concentrations associated with arctic haze in springtime cold-air outbreaks. *Atmospheric Chemistry and Physics*, *24*(24), 14045–14072. https://doi.org/10.5194/acp-24-14045-2024

Rotstayn, L. D., Ryan, B. F., & Katzfey, J. J. (2000). A scheme for calculation of the liquid fraction in mixed-phase stratiform clouds in large-scale models. *Monthly Weather Review*, *128*, 1070–1088. https://doi.org/10.1175/1520-0493(2000)128⟨1070:ASFCOT⟩2.0.CO;2

Seifert, A., & Siewert, C. (2024). An ml-based p3-like multimodal two-moment ice microphysics in the icon model. *Journal of Advances in Modeling Earth Systems*, *16*(8), e2023MS004206. https://doi.org/10.1029/2023MS004206

Sokol, A. B., & Storelvmo, T. (2024). The spatial heterogeneity of cloud phase observed by satellite. *Journal of Geophysical Research: Atmospheres*, *129*(3), e2023JD039751. https://doi.org/10.1029/2023JD039751

Sorooshian, A., Anderson, B., Bauer, S. E., Braun, R. A., Cairns, B., Crosbie, E., et al. (2019). Aerosol–cloud–meteorology interaction airborne field investigations: Using lessons learned from the u.s. west coast in the design of activate off the u.s. east coast. *Bulletin America Meteorology Social*, *100*(8), 1511–1528. https://doi.org/10.1175/bams-d-18-0100.1

Tan, I., & Barahona, D. (2022). The impacts of immersion ice nucleation parameterizations on arctic mixed-phase stratiform cloud properties and the arctic radiation budget in geos-5. *Journal of Climate*, *35*(13), 4049–4070. https://doi.org/10.1175/JCLI-D-21-0368.1

Tan, I., & Storelvmo, T. (2019). Evidence of strong contributions from mixed-phase clouds to arctic climate change. *Geophysical Research Letters*, *46*(5), 2894–2902. https://doi.org/10.1029/2018GL081871

Tan, I., Storelvmo, T., & Zelinka, M. D. (2016). Observational constraints on mixed-phase clouds imply higher climate sensitivity. *Science*, *352*(6282), 224–227. https://doi.org/10.1126/science.aad5300

Tomassini, L., Field, P. R., Honnert, R., Malardel, S., McTaggart-Cowan, R., Saitou, K., et al. (2017). The "grey zone" cold air outbreak global model intercomparison: A cross evaluation using large-eddy simulations. *Journal of Advances in Modeling Earth Systems*, *9*(1), 39–64. https://doi.org/10.1002/2016MS000822

Turbeville, S. M., Nugent, J. M., Ackerman, T. P., Bretherton, C. S., & Blossey, P. N. (2022). Tropical cirrus in global storm-resolving models: 2. cirrus life cycle and top-of-atmosphere radiative fluxes. *Earth and Space Science*, *9*(2), e2021EA001978. https://doi.org/10.1029/2021EA001978

Van Weverberg, K., Giangrande, S., Zhang, D., Morcrette, C. J., & Field, P. R. (2023). On the role of macrophysics and microphysics in km-scale simulations of mixed-phase clouds during cold air outbreaks. *Journal of Geophysical Research: Atmospheres*, *128*(11), e2022JD037854. https://doi.org/10.1029/2022JD037854

Verlinde, J., Harrington, J. Y. M. M. G., McFarquhar, G. M., Yannuzzi, V. T., Avramov, A., Greenberg, S., et al. (2007). The mixed-phase arctic cloud experiment. *Bulletin America Meteorology Social*, *88*(2), 205–222. https://doi.org/10.1175/bams-88-2-205

Welti, A., Bigg, E. K., DeMott, P. J., Gong, X., Hartmann, M., Harvey, M., et al. (2020). Ship-based measurements of ice nuclei concentrations over the arctic, atlantic, pacific and southern oceans. *Atmospheric Chemistry and Physics*, *20*(23), 15191–15206. https://doi.org/10.5194/acp-20-15191-2020

Wendisch, M., Crewell, S., Ehrlich, A., Herber, A., Kirbus, B., Lüpkes, C., et al. (2024). Overview: Quasi-lagrangian observations of arctic air mass transformations – Introduction and initial results of the halo–(ac)3 aircraft campaign. *Atmospheric Chemistry and Physics*, *24*(15), 8865–8892. https://doi.org/10.5194/acp-24-8865-2024

Westbrook, C. D., & Illingworth, A. J. (2011). Evidence that ice forms primarily in supercooled liquid clouds at temperatures¿ 27°c. *Geophysical Research Letters*, *38*(14). https://doi.org/10.1029/2011GL048021

Williams, A. S., Dedrick, J. L., Russell, L. M., Tornow, F., Silber, I., Fridlind, A. M., et al. (2024). Aerosol size distribution properties associated with cold-air outbreaks in the norwegian arctic. *Atmospheric Chemistry and Physics*, *24*(20), 11791–11805. https://doi.org/10.5194/acp-24-11791-2024

Wu, P., & Ovchinnikov, M. (2022). Cloud morphology evolution in arctic cold-air outbreak: Two cases during comble period. *Journal of Geophysical Research: Atmospheres*, *127*(10), e2021JD035966. https://doi.org/10.1029/2021JD035966

Wu, P., Ovchinnikov, M., Xiao, H., Lackner, C. P., Geerts, B., Tornow, F., & Elsaesser, G. (2025). Effect of ice number concentration on the evolution of boundary layer clouds during arctic marine cold-air outbreaks. *Journal of Geophysical Research: Atmospheres*, *130*(3), e2024JD041282. https://doi.org/10.1029/2024JD041282

Yang, J., Lu, J., Deng, Y., Wang, Y., Lu, C., Yin, Y., et al. (2025). Parameterizing the heterogeneous liquid-ice mixing in modeling ice growth through the wegener-bergeron-findeisen process in cam6. *Geophysical Research Letters*, *52*(7), e2024GL114036. https://doi.org/10.1029/2024GL114036

Zelinka, M. D., Myers, T. A., McCoy, D. T., Po-Chedley, S., Caldwell, P. M., Ceppi, P., et al. (2020). Causes of higher climate sensitivity in cmip6 models. *Geophysical Research Letters*, *47*(1), e2019GL085782. https://doi.org/10.1029/2019GL085782

Zhang, M., Liu, X., Diao, M., D'Alessandro, J. J., Wang, Y., Wu, C., et al. (2019). Impacts of representing heterogeneous distribution of cloud liquid and ice on phase partitioning of arctic mixed-phase clouds with ncar cam5. *Journal of Geophysical Research: Atmospheres*, *124*(23), 13071–13090. https://doi.org/10.1029/2019JD030502

Zheng, X., Zhang, Y., Klein, S. A., Zhang, M., Zhang, Z., Deng, M., et al. (2024). Using satellite and arm observations to evaluate cold air outbreak cloud transitions in e3sm global storm-resolving simulations. *Geophysical Research Letters*, *51*(8), e2024GL109175. https://doi.org/10.1029/2024GL109175